Stalling of Globular Cluster Orbits in Dwarf Galaxies

Karamveer Kaur and S. Sridhar

Raman Research Institute, Sadashivanagar, Bangalore 560 080, India; karamveer@rri.res.in, ssridhar@rri.res.in
Received 2018 September 29; accepted 2018 October 18; published 2018 December 3

Abstract

We apply the Tremaine–Weinberg theory of dynamical friction to compute the orbital decay of a globular cluster (GC) on an initially circular orbit inside a cored spherical galaxy with isotropic stellar velocities. The retarding torque on the GC, $\mathcal{T}(r_p) < 0$, is a function of its orbital radius r_p. The torque is exerted by stars whose orbits are resonant with the GC's orbit and given as a sum over the infinitely many possible resonances by the Lynden-Bell–Kalnajs (LBK) formula. We calculate the LBK torque $\mathcal{T}(r_p)$ and determine $r_p(t)$ for a GC of mass $M_p = 2 \times 10^5 \, M_\odot$ and an isochrone galaxy of core mass $M_c = 4 \times 10^8 \, M_\odot$ and core radius $b = 1000$ pc. (i) When $r_p \gtrsim 300$ pc, many strong resonances are active, and as expected, $\mathcal{T} \approx \mathcal{T}_C$, the classical Chandrasekhar torque. (ii) For $r_p < 300$ pc, $\mathcal{T}$ comes mostly from stars nearly corotating with the GC, trailing or leading it slightly; trailing resonances exert stronger torques. (iii) As r_p decreases, the number and strength of resonances drop, so $|\mathcal{T}|$ also decreases, with $|\mathcal{T}| < 10^{-2} |\mathcal{T}_C|$ at $r_p = r_* \simeq (M_p/M_c)^{1/5} b \simeq 220$ pc, a characteristic "filtering" radius. (iv) Many resonances cease to exist inside r_*; this includes all leading and low-order trailing ones. (v) The higher-order trailing resonances inside r_* are very weak, with $|\mathcal{T}| < 10^{-4} |\mathcal{T}_C|$ at $r_p = 150$ pc. (vi) Inspiral times for $r_p(t)$ to decay from 300 pc to r_* far exceed 10 Gyr.

Key words: galaxies: dwarf – galaxies: kinematics and dynamics

1. Introduction

A globular cluster (GC) orbiting a galaxy experiences dynamical friction, the drag exerted by the gravity of the wake it generates in the galaxy. Chandrasekhar (1943) derived a formula for the drag on a perturber moving through an infinite and homogeneous sea of stars with isotropic velocity distribution. When applied as a local approximation to a GC of mass M_p moving with velocity v_p inside a spherical galaxy, the Chandrasekhar dynamical friction formula for the drag force is

$$M_p \frac{dv_p}{dt} = -4\pi \, G^2 M_p^2 \, \ln\Lambda \, \rho(r_p; v < v_p) \frac{v_p}{v_p^3}. \quad (1)$$

Here, r_p is the GC's orbital radius, $\rho(r_p; v < v_p)$ is the mass density at r_p of stars and dark matter with speeds less than the GC's speed, and $\ln\Lambda$ is the Coulomb logarithm (Binney & Tremaine 2008). This drag causes the loss of the GC's orbital angular momentum, making it sink toward the galactic center. The effect is so strong in dwarf galaxies that a GC on an initially circular orbit is expected to sink to the galactic center within a few Gyr (Tremaine 1976; Hernandez & Gilmore 1998; Oh et al. 2000; Vesperini 2000, 2001; Goerdt et al. 2006). But many dwarf galaxies host GCs that are old (e.g., Durrell et al. 1996; Miller et al. 1998; Lotz et al. 2004). A particularly good example is the Fornax dwarf spheroidal galaxy with five old metal-poor GCs (Buonanno et al. 1998, 1999; Mackey & Gilmore 2003; Strader et al. 2003; Greco et al. 2007), already noted in Tremaine (1976). Why are these GCs observed so far away from their galactic centers?

Work over the past two decades on this "dynamical friction problem" suggests that the orbits of GCs (or other compact masses) can indeed stall in the core regions of a dwarf galaxy. Hernandez & Gilmore (1998) used the Chandrasekhar formula for a King model halo to argue that dynamical friction weakens in the core region of a galaxy. Numerical simulations exploring

core-stalling as a function of the cored/cuspy nature of the galaxy's inner density profile have shown that a nearly constant density core would result in core-stalling (Goerdt et al. 2006; Read et al. 2006; Cole et al. 2012). Analogous core-stalling of a supermassive black hole was studied by Gualandris & Merritt (2008). Numerical simulations by Inoue (2009, 2011) are particularly revealing, with Inoue (2011, hereafter In11) providing the deepest insights through the analysis of a single numerical experiment. A semi-analytical model based on the Chandrasekhar formula for cored galaxies has been offered by Petts et al. (2016). The physical explanations advanced differ from each other, but all agree that dynamical friction is highly suppressed and can even be zero in galaxies with a nearly constant density core. Both Read et al. (2006) and In11 emphasized the role of "corotating" particles in the suppression of dynamical friction, but the term seems to refer to qualitatively different orbits. The goal of this paper is to seek a physical interpretation of the GC stalling phenomenon in terms of the standard theory of dynamical friction in spherical stellar systems due to Tremaine & Weinberg (1984, hereafter TW84), explored further in Weinberg (1986, 1989).

Physical setting of TW84. The stars and dark matter in the galaxy can be considered to be "collisionless" over Hubble timescales, so they respond similarly to gravitational fields (Binney & Tremaine 2008). The galaxy is described by a mass distribution function (DF) in six-dimensional position–velocity phase space. Each mass element (henceforth referred to as a "star") orbits in the combined gravitational fields of all the other stars and the GC. In the spherically symmetric potential of the unperturbed galaxy, a stellar orbit is a "rosette" confined to a plane, with radial and angular frequencies that are functions only of E (the orbital energy per unit mass) and L (the magnitude of the angular momentum per unit mass). The GC is initially on a circular orbit in the x–y plane. Its gravitational attraction perturbs and rearranges the distribution of mass in the galaxy, with an associated change in the z-component of the

angular momentum of the galaxy. The torque on the GC is equal and opposite to the rate at which angular momentum is absorbed by the galaxy.

The rate of absorption of angular momentum by the galaxy can be positive or negative. When the perturbation is very weak (strictly infinitesimal), angular momentum is absorbed by those "rosette" orbits whose radial and angular frequencies are in resonance with the GC's orbital frequency. Resonances are characterized by a triplet of integers, one each for the three frequencies. Each resonance is a five-dimensional surface in phase space. As the three integers run over all possible values, the set of resonant surfaces covers the phase space densely. Angular momentum exchanges with the GC can be thought of as occurring on resonant surfaces. The sum of the torques exerted by all the resonances is equal to the net torque, referred to as the "Lynden-Bell–Kalnajs (LBK) torque" by TW84, who generalized an earlier derivation by Lynden-Bell & Kalnajs (1972) for two-dimensional disks. This is valid in the linear limit of perturbation theory.[1] The simplest model of a stable, spherical galaxy is an isotropic DF, $F(E)$ with $(dF/dE) < 0$, corresponding to the DF from which the initial conditions of In11 were drawn. TW84 noted the important point that in this case, the torque due to each resonance is always retarding. Therefore, linear theory predicts that the GC will inspiral toward the galactic center. The questions of interest are as follows. As the GC inspirals, what are the resonances available to it? How large are the resonant torques? What is the rate of orbital decay due to the net LBK torque?

Going forward with TW84. When the GC's orbit lies outside the core of the galaxy, there is a dense set of resonances available to it. TW84 noted that, in the limit the resonances form a continuum, the LBK torque should reduce to the Chandrasekhar torque (with a suitable choice of the Coulomb logarithm). The corresponding orbital decay can be seen in the In11 simulation of a GC of mass $2 \times 10^5 \, M_\odot$, set on a circular orbit with an initial radius of 750 pc, inside a spherical galaxy of mass $2 \times 10^9 \, M_\odot$ and core radius 1000 pc. During the initial 4 Gyr, the GC's orbital radius decreased from 750 to 300 pc, in rough agreement with the action of the Chandrasekhar formula. Thereafter, its behavior departed drastically from the formula's prediction: the rate of decrease slows down dramatically, and the radius stalls around a mean value of about 225 pc until the end of the simulation at 10 Gyr. We are interested in understanding this stalling phenomenon.

Let us imagine—contrary to In11—that the GC has some-how managed to reach close to the galaxy's center. In a limiting sense, the GC has entered a constant density environment where the galaxy's potential $\propto r^2$ (an isotropic harmonic oscillator), so every stellar orbit is a centered ellipse with the same orbital frequency, independent of shape, size, or orientation. Then, either all stars are resonant (and the response is singular) or no star is resonant and the LBK torque would vanish. TW84 remarked that in realistic systems, the density is not quite constant, so there will always be some resonances and the response will be finite. Hence, a constant density core is a pathological case. But it does illustrate the point that, were the GC to reach the very central regions of the galaxy, there would likely be no resonant stars and hence no friction. This line of thought suggests the following physical picture of core-stalling in a realistic galaxy core with a varying central density profile.

As the GC inspirals from a radius of 300 pc, there are progressively fewer strong resonances available for it to exchange angular momentum with the galaxy. Since only a small fraction of the core stars would then be involved in the resonant exchange, the LBK torque exerted on the GC could be so suppressed that the rate of orbital decay to the center may take much longer than a Hubble time.

Plan of the paper. Section 2 gives a brief account of the part of TW84 that is used in this paper. We set notation describing galaxies and linear perturbations, introduce action-angle variables specially adapted for studying core dynamics later, and give a short derivation of TW84's LBK torque formula, in the spirit of Kalnajs (1971). In Section 3, the unperturbed galaxy is represented by an isochrone model and described by action-angle variables in the rotating frame of the GC. Isochrone parameters are chosen by comparison with those used by In11. We compute the orbital decay of the GC according to the Chandrasekhar torque for the isochrone—this serves as a useful benchmark for later comparison with decay due to the LBK torque. The GC is modeled as a Plummer sphere whose tidal potential needs to be expressed in terms of the isochrone action-angle variables using the formulae for the three-dimensional orbit in space. Expressions for the resonant torques and LBK torque are recorded.

Section 4 takes a close look at the structure of resonances in the isochrone core. Core orbits are worked out, and a natural small parameter is identified. The orbital and precessional frequencies are compared with the GC's orbital frequency, yielding a characteristic radius, r_*. Torques are written in dimensionless action-angle variables. Core resonances are classified as *corotating* and *non-corotating*, with the latter consisting of higher-order, weaker resonances. Corotating resonances come in two types, trailing and leading, both of which are explored in Section 5 as functions of r_p, the orbital radius of the GC. The associated torque integrals, derived in the previous section, are now computed numerically. The progressive culling of low-order resonances as r_p decreases is followed in detail, and the role of r_* as a "filtering" radius for resonances is clarified. Resonant torques are then summed over to obtain the net trailing and leading torques; the LBK torque is the sum of these two torques.

In Section 6, we discuss leading and trailing torque profiles, compute the orbital decay of the GC according to the LBK torque, and compare this with the orbital decay due to the Chandrasekhar torque studied earlier. We conclude in Section 7.

2. Tremaine–Weinberg Theory

2.1. Collisionless Dynamics of the Galaxy

We begin with a brief account of the dynamical framework that is used in the construction of our model; see Binney & Tremaine (2008) for a comprehensive account. Let $\boldsymbol{x}$ be the position vector of a star and $\boldsymbol{v}$ its velocity vector with respect to an inertial frame. The galaxy is described by a DF, $f(\boldsymbol{x}, \boldsymbol{v}, t)$, which is equal to the mass density at time t in the six-dimensional $\{\boldsymbol{x}, \boldsymbol{v}\}$ phase space. Here, f is nonnegative and normalized as

$$\int d\boldsymbol{x} \, d\boldsymbol{v} \, f(\boldsymbol{x}, \boldsymbol{v}, t) = M, \qquad (2)$$

where M is the total mass of the galaxy. The time evolution of the DF is governed by the collisionless Boltzmann equation (CBE),

$$\frac{df}{dt} \equiv \frac{\partial f}{\partial t} + \boldsymbol{v} \cdot \frac{\partial f}{\partial \boldsymbol{x}} - \frac{\partial \Phi^{\mathrm{tot}}}{\partial \boldsymbol{x}} \cdot \frac{\partial f}{\partial \boldsymbol{v}} = 0,$$

---

[1] TW84 also studied the nonlinear dynamics of resonances and discussed orbit capture into resonant islands. This is beyond the scope of this paper.

where $\Phi^{\rm tot}(\boldsymbol{x}, t)$ is the total gravitational potential, equal to the sum of the potentials due to the self-gravity of the galaxy and any external perturbing sources,

$$\Phi^{\rm tot}(\boldsymbol{x}, t) = \Phi(\boldsymbol{x}, t) + \Phi^{\rm ext}(\boldsymbol{x}, t), \qquad (3)$$

where

$$\Phi(\boldsymbol{x}, t) = -G \int d\boldsymbol{x}' \, d\boldsymbol{v}' \, \frac{f(\boldsymbol{x}', \boldsymbol{v}', t)}{|\boldsymbol{x} - \boldsymbol{x}'|} \qquad (4)$$

is the self-consistent Newtonian potential. The external potential, $\Phi^{\rm ext}(\boldsymbol{x}, t)$, depends on what dynamical process is being studied. It could be due to galactic bars, spiral density waves, or infalling objects such as satellite galaxies, GCs, or massive black holes.

The CBE can be rewritten compactly as

$$\frac{\partial f}{\partial t} + [f, H] = 0, \qquad (5)$$

where H is the Hamiltonian (equal to the orbital energy per unit mass),

$$H(\boldsymbol{x}, \boldsymbol{v}, t) = \frac{v^2}{2} + \Phi^{\rm tot}(\boldsymbol{x}, t), \qquad (6)$$

and

$$[f, H] = \frac{\partial f}{\partial \boldsymbol{x}} \cdot \frac{\partial H}{\partial \boldsymbol{v}} - \frac{\partial f}{\partial \boldsymbol{v}} \cdot \frac{\partial H}{\partial \boldsymbol{x}} \qquad (7)$$

is the Poisson bracket between the phase-space functions, f and H. This form of the CBE is particularly useful because the Poisson bracket remains invariant when we later transform from the $\{\boldsymbol{x}, \boldsymbol{v}\}$ to other canonically conjugate variables.

An isolated, unperturbed galaxy is often described by a time-independent DF, $f_0(\boldsymbol{x}, \boldsymbol{v})$. Let $\Phi_0(\boldsymbol{x})$ be the galaxy's self-consistent potential, related to f_0 through Equation (4). Then, the unperturbed Hamiltonian is

$$H_0(\boldsymbol{x}, \boldsymbol{v}) = \frac{v^2}{2} + \Phi_0(\boldsymbol{x}). \qquad (8)$$

Because f_0 solves the CBE, we must have $[f_0, H_0] = 0$, so f_0 is a function of the isolating integrals of motion of H_0 (the Jeans theorem). For any given function of the integrals, one needs to solve the self-consistent problem of Equation (4) to determine f_0 as a function of $(\boldsymbol{x}, \boldsymbol{v})$.

Let $f_1(\boldsymbol{x}, \boldsymbol{v}, t)$ be a small perturbation to f_0, either due to fluctuations in the initial conditions or forced through weak external gravitational fields. In either case, there is a corresponding perturbation to the self-gravitational potential, $\Phi_1(\boldsymbol{x}, t)$, which is related to f_1 through Equation (4). Including a weak external potential, $\Phi_1^{\rm ext}(\boldsymbol{x}, t)$, the perturbation to the Hamiltonian is $H_1(\boldsymbol{x}, t) = \Phi_1(\boldsymbol{x}, t) + \Phi_1^{\rm ext}(\boldsymbol{x}, t)$. The total DF, $f = f_0 + f_1$, must obey the CBE with the total Hamiltonian, $H = H_0 + H_1$. In the limit of an infinitesimally small perturbation, f_1 obeys the linearized CBE (LCBE),

$$\frac{\partial f_1}{\partial t} + [f_1, H_0] + [f_0, H_1] = 0, \qquad (9)$$

where the second-order term, $[f_1, H_1]$, has been neglected. It is necessary for the unperturbed galaxy to be linearly stable in the absence of external perturbations. In other words, the LCBE with $H_1 = \Phi_1$ should not admit solutions, f_1, that are exponentially growing in time; then, f_0 is said to be a linearly stable DF.

While considering the response of such a stable DF to $\Phi_1^{\rm ext} \neq 0$, TW84 neglected "gravitational polarization" effects and set $\Phi_1 = 0$. Then, $H_1 = \Phi_1^{\rm ext}$, and the LCBE governing the "passive response" of the galaxy to the perturber is

$$\frac{\partial f_1}{\partial t} + [f_1, H_0] + [f_0, \Phi_1^{\rm ext}] = 0. \qquad (10)$$

There is no real justification for the neglect of Φ_1 besides the fact that, by so doing one has to deal only with a partial differential equation, instead of an integral equation. We follow TW84 and use Equation (10) to compute the linear response of the galaxy.[2]

2.2. Unperturbed Galaxy

We use spherical polar coordinates to describe the unperturbed spherical galaxy. Let $\boldsymbol{r} = (r, \theta, \phi)$ be the position vector with respect to the galactic center. The unperturbed potential, $\Phi_0(r)$, is a function of only r. The canonically conjugate momenta are $\boldsymbol{p} = (p_r, p_\theta, p_\phi)$, where $p_r = \dot{r}$ is the radial velocity, $p_\theta = r^2\dot{\theta}$, and $p_\phi = r^2 \sin^2\theta \dot{\phi} = \hat{z} \cdot (\boldsymbol{r} \times \boldsymbol{p}) = L_z$ is the z-component of the angular momentum per unit mass. The magnitude of the angular momentum per unit mass is $L = \sqrt{p_\theta^2 + p_\phi^2 / \sin^2\theta}$. The unperturbed Hamiltonian,

$$H_0(\boldsymbol{r}, \boldsymbol{p}) = \frac{1}{2}\left(p_r^2 + \frac{p_\theta^2}{r^2} + \frac{p_\phi^2}{r^2 \sin^2\theta}\right) + \Phi_0(r), \qquad (11)$$

which is equal to the energy per unit mass (E), governs the dynamics of a star. An orbit is confined to an invariant plane passing through the origin, which is inclined to the x–y plane by angle i. Here (E, L, L_z) are constant along the orbit, with $\cos i = L_z/L$. The radial and angular frequencies of the orbit in its plane, $\Omega_r(E, L)$ and $\Omega_\psi(E, L)$, respectively, are generally incommensurate. Hence, a generic orbit describes a "rosette" as it goes through many periapse and apoapse passages, filling an annular disk. Since (E, L, L_z) are also isolating integrals of motions, the Jeans theorem implies that any spherical unperturbed DF must be a function of these three integrals. A nonrotating galaxy with complete spherical symmetry in phase space must have a DF, $f_0 = F(E, L)$, that is independent of L_z; such a DF has zero streaming velocities with, in general, anisotropic velocity dispersion. The subclass, $f_0 = F(E)$, has isotropic velocity dispersion and is linearly stable to all perturbations when $(dF/dE) < 0$; these are the models relevant to the In11 simulation.

---

[2] Kalnajs (1972) argued that gravitational polarization effects in a uniformly rotating sheet can suppress dynamical friction and showed that the frictional force on a perturber on a circular orbit is zero. Indeed, polarization effects can be important. But the demonstration of the strict vanishing of frictional force is limited by the fact that the dynamical response of a uniformly rotating sheet is as pathological as the strictly constant density galactic core, discussed earlier in the Introduction.

We can transform from $\{r, p\}$ to new canonical variables, $\{w, I\}$, where $w = (w_1, w_2, w_3)$ are three coordinates called "angles" and $I = (I_1, I_2, I_3)$ are their conjugate momenta called "actions" (see Binney & Tremaine 2008, Section 3.5.2). There are many equivalent choices of action-angle variables. The standard "primitive" variables, also used by TW84, are

$$I_1 = J_r = \text{radial action}, \quad w_1 = \Omega_r(t - t_p), \quad (12a)$$

$$I_2 = L, \quad w_2 = \chi + \Omega_\psi(t - t_p), \quad (12b)$$

$$I_3 = L_z, \quad w_3 = h. \quad (12c)$$

Here, h is the longitude of the ascending node, and χ is the angle from the ascending node to a periapse that is visited at time t_p. An alternative set of actions and angles is

$$I_1 = 2J_r + L, \quad w_1 = \frac{\Omega_r}{2}(t - t_p), \quad (13a)$$

$$I_2 = L, \quad w_2 = \chi + \left(\Omega_\psi - \frac{\Omega_r}{2}\right)(t - t_p), \quad (13b)$$

$$I_3 = L_z, \quad w_3 = h. \quad (13c)$$

This proves particularly useful for the exploration of the dynamics of core stars, for which $\Omega_r \simeq 2\Omega_\psi$, making w_2 a slowly varying angle compared to w_1. This is the choice made from Section 3 onward. But in this section, $\{w, I\}$ will stand for either set of variables, defined by Equations (12) or (13), both giving completely equivalent descriptions of dynamics over all of phase space.

The Hamiltonian is independent of L_z and can be written as $H_0(I_1, I_2)$. Hamilton's equations of motion, $dw/dt = \partial H_0/\partial I$ and $dI/dt = -\partial H_0/\partial w$, imply that the actions I are constants of motion and the angles advance at constant rates, with $w_3 = h$ being fixed. The unperturbed DF, $f_0 = F_0(I_1, I_2)$, describes a spherically symmetric, nonrotating system with anisotropic velocity dispersion. The subclass with isotropic velocity dispersion will be written as $f_0 = F_0(H_0)$.

2.3. Dynamics in the Rotating Frame of the Perturber

The galaxy is acted upon by an external rotating potential perturbation of the form $\Phi_1^{\text{ext}}(r, \theta, \phi - \xi(t))$, where $d\xi(t)/dt = \Omega_p(t)$ is the time-dependent angular frequency of rotation about the $\hat{z}$-axis. This could arise from a galactic bar or GC on a circular orbit in the x–y plane. TW84 studied the effect of bar-like perturbations whose symmetry is such that it does not change the location of the center of mass of the galaxy. We are interested in the latter case, where the GC and the galaxy orbit each other in circles about a common and fixed center of mass. This motion of the center of the galaxy must be accounted for by choosing Φ_1^{ext} as the "tidal," rather than the "bare," potential of the perturber; this is done in Section 3. However, in either case, the potential perturbation is of the above form. In a frame that rotates with angular velocity $\hat{z}\Omega_p(t)$, the perturbation would appear stationary, so this is the preferred frame for the formulation of stellar dynamics.

Henceforth, we use $r = (r, \theta, \phi)$ for the position vector in the rotating frame, with origin at the center of the galaxy, and $p = (p_r, p_\theta, p_\phi = L_z)$ to denote its conjugate momentum. In the rotating frame, the line of nodes of every unperturbed orbit (regardless of its size, shape, or orientation) regresses at the common angular rate, $\Omega_p(t)$. This can be taken into account by subtracting $\Omega_p(t)I_3$ from H_0 to obtain the Jacobi Hamiltonian

for unperturbed dynamics:

$$H_{J0}(I_1, I_2, I_3, t) = H_0(I_1, I_2) - \Omega_p(t)I_3. \quad (14)$$

The unperturbed frequencies in the rotating frame are

$$\frac{dw_1}{dt} \equiv \Omega_1(I_1, I_2) = \frac{\partial H_{J0}}{\partial I_1} = \frac{\partial H_0}{\partial I_1}, \quad (15a)$$

$$\frac{dw_2}{dt} \equiv \Omega_2(I_1, I_2) = \frac{\partial H_{J0}}{\partial I_2} = \frac{\partial H_0}{\partial I_2}, \quad (15b)$$

and

$$\frac{dw_3}{dt} \equiv \Omega_3 = \frac{\partial H_{J0}}{\partial I_3} = -\Omega_p(t). \quad (15c)$$

The time dependence of $\Omega_p(t)$ is due to the back-reacting torque the galaxy exerts on the perturber and is slow compared to orbital times.[3] Henceforth, we drop the explicit time dependence in Ω_p and treat $H_{J0}(I_1, I_2, I_3)$ as an adiabatically varying Hamiltonian.

The perturbation is applied gradually in time in order to eliminate transients in the response of the galaxy: the standard manner of ensuring this is to set $\Phi_1^{\text{ext}} = \exp(\gamma t)\Phi_p(r)$, where $\gamma > 0$ can be taken to zero at the end of the calculation. Writing $f_1 = \exp(\gamma t)F_1(r, p)$ and substituting for f_1 and Φ_1^{ext} in the passive response LCBE (Equation (10)), we obtain

$$\gamma F_1 + [F_1, H_{J0}] + [F_0, \Phi_p] = 0, \quad (16)$$

where we have replaced H_0 by the adiabatically varying Jacobi Hamiltonian of Equation (14). The Poisson brackets in terms of the $\{w, I\}$ variables are

$$[F_1, H_{J0}] = \Omega_1 \frac{\partial F_1}{\partial w_1} + \Omega_2 \frac{\partial F_1}{\partial w_2} - \Omega_p \frac{\partial F_1}{\partial w_3}, \quad (17a)$$

$$[F_0, \Phi_p] = -\frac{\partial F_0}{\partial I_1} \frac{\partial \Phi_p}{\partial w_1} - \frac{\partial F_0}{\partial I_2} \frac{\partial \Phi_p}{\partial w_2}. \quad (17b)$$

We expand F_1 and Φ_p as Fourier series in the angles

$$F_1 = \sum_{l_1, l_2, l_3} \widetilde{F}_{l_1 l_2 l_3}(I) \exp\{i(l \cdot w)\}, \quad (18a)$$

$$\Phi_p = \sum_{l_1, l_2, l_3} \widetilde{\Phi}_{l_1 l_2 l_3}(I) \exp\{i(l \cdot w)\}, \quad (18b)$$

where the sum is over all integer triplets (l_1, l_2, l_3), and $l \cdot w = l_1 w_1 + l_2 w_2 + l_3 w_3$. Since F_1 and Φ_p are real quantities, we must have $\widetilde{F}_{-l_1, -l_2, -l_3} = \widetilde{F}_{l_1 l_2 l_3}^*$ and $\widetilde{\Phi}_{-l_1, -l_2, -l_3} = \widetilde{\Phi}_{l_1 l_2 l_3}^*$. Substituting Equations 17(a)–18(b) in Equation (16) and solving for $\widetilde{F}_{l_1 l_2 l_3}$, we obtain

$$\widetilde{F}_{l_1 l_2 l_3}(I) = \left(l_1 \frac{\partial F_0}{\partial I_1} + l_2 \frac{\partial F_0}{\partial I_2}\right)$$
$$\times \frac{i\,\widetilde{\Phi}_{l_1 l_2 l_3}(I)}{[\gamma + i(l_1 \Omega_1 + l_2 \Omega_2 - l_3 \Omega_p)]} \quad (19)$$

as the linear response of the galaxy to the imposed perturbation when polarization effects are ignored.

2.4. The LBK Formula

TW84 derived the LBK torque formula by computing the change in the z-component of the angular momentum of individual orbits and then summing over the contributions of all orbits. Their method is an extension of Lynden-Bell & Kalnajs (1972) to spherical systems and requires calculating the angular momentum changes to second order in the perturbation. However, the original derivation for flat disks by Kalnajs (1971) only requires the first-order change in the DF and does not need computation of individual orbits to second order. Below, we present a short and simple derivation of the LBK formula for spherical systems in the spirit of Kalnajs (1971). The z-component of the torque exerted by the galaxy on the perturber is equal and opposite to the torque exerted by the perturber on the galaxy. Hence, the LBK torque on the perturber is

$$\mathcal{T} = \int d\boldsymbol{r}\, d\boldsymbol{p} \frac{\partial \Phi_1^{\mathrm{ext}}}{\partial \phi}\{f_0 + f_1\} = \int d\boldsymbol{r}\, d\boldsymbol{p} \frac{\partial \Phi_1^{\mathrm{ext}}}{\partial \phi} f_1. \quad (20)$$

It is second order in the perturbation because f_0 is independent of ϕ and $\oint d\phi\,(\partial\Phi_1^{\mathrm{ext}}/\partial\phi) = 0$. The decisive step is to note that $(\partial\Phi_1^{\mathrm{ext}}/\partial\phi) = -[p_\phi, \Phi_1^{\mathrm{ext}}] = -[L_z, \Phi_1^{\mathrm{ext}}]$ and use the invariance of the Poisson bracket to rewrite Equation (20) in terms of action-angle variables:

$$\mathcal{T} = -\int d\boldsymbol{w}\, d\boldsymbol{I}\,[I_3, \Phi_1^{\mathrm{ext}}] f_1 = \exp(2\gamma t) \int d\boldsymbol{w}\, d\boldsymbol{I}\, \frac{\partial \Phi_{\mathrm{p}}}{\partial w_3} F_1$$
$$= 8\pi^3 \exp(2\gamma t) \sum_{l_1,l_2,l_3} i l_3 \int d\boldsymbol{I}\, \widetilde{\Phi}_{l_1 l_2 l_3}(\boldsymbol{I}) \widetilde{F}^*_{l_1 l_2 l_3}(\boldsymbol{I}). \quad (21)$$

Using Equation (19) to express $\widetilde{F}^*_{l_1 l_2 l_3}$ in terms of $\widetilde{\Phi}^*_{l_1 l_2 l_3}$,

$$\mathcal{T} = 8\pi^3 \exp(2\gamma t) \sum_{l_1,l_2,l_3} l_3 \int d\boldsymbol{I} \left(l_1 \frac{\partial F_0}{\partial I_1} + l_2 \frac{\partial F_0}{\partial I_2} \right)$$
$$\times \frac{|\widetilde{\Phi}_{l_1 l_2 l_3}(\boldsymbol{I})|^2}{[\gamma - i(l_1\Omega_1 + l_2\Omega_2 - l_3\Omega_{\mathrm{p}})]}. \quad (22)$$

In the limit $\gamma \to 0_+$, we have

$$[\gamma - i(l_1\Omega_1 + l_2\Omega_2 - l_3\Omega_{\mathrm{p}})]^{-1} \rightarrow$$
$$i(l_1\Omega_1 + l_2\Omega_2 - l_3\Omega_{\mathrm{p}})^{-1} + \pi\,\delta(l_1\Omega_1 + l_2\Omega_2 - l_3\Omega_{\mathrm{p}}),$$

where $\delta(\ )$ is the Dirac δ-function that picks out resonances. The first term on the right side is purely imaginary and cannot contribute to the torque, which is a real quantity; and indeed it does not, as can be seen by noting that the (l_1, l_2, l_3) term is canceled by the $(-l_1, -l_2, -l_3)$ term because $|\widetilde{\Phi}_{l_1 l_2 l_3}(\boldsymbol{I})|^2 = |\widetilde{\Phi}_{-l_1, -l_2, -l_3}(\boldsymbol{I})|^2$. On the other hand, both terms add for the δ-function contribution. Therefore, we arrive at the LBK formula for the torque:[4]

$$\mathcal{T} = \sum_{l_1,l_2 = -\infty}^{\infty} \sum_{l_3 = 1}^{\infty} \mathcal{T}_{l_1 l_2 l_3}, \qquad \text{where} \qquad (23a)$$

$$\mathcal{T}_{l_1 l_2 l_3} = 16\pi^4\, l_3 \int d\boldsymbol{I} \left(l_1 \frac{\partial F_0}{\partial I_1} + l_2 \frac{\partial F_0}{\partial I_2} \right)$$
$$\times \delta(l_1\Omega_1 + l_2\Omega_2 - l_3\Omega_{\mathrm{p}})|\widetilde{\Phi}_{l_1 l_2 l_3}(\boldsymbol{I})|^2. \quad (23b)$$

The total torque acting on the perturber is the sum of the torques exerted by all the resonant surfaces. Each resonant surface is a five-dimensional subspace of six-dimensional phase space defined by the resonance condition,

$$l_1\Omega_1(I_1, I_2) + l_2\Omega_2(I_1, I_2) - l_3\Omega_{\mathrm{p}} = 0, \quad (24)$$

for any specified integer triplet, $(l_1, l_2, l_3 > 0)$. The resonance condition is independent of the third action, $I_3 = L_z$, because the unperturbed galaxy is spherical.

The unperturbed galaxy relevant to the In11 simulation is represented by a stable, spherical DF with isotropic velocity dispersions of the form $F_0(E)$ with $dF_0/dE < 0$. TW84 made the important point that the LBK torque is always retarding. To see this, we note that

$$\left(l_1 \frac{\partial F_0}{\partial I_1} + l_2 \frac{\partial F_0}{\partial I_2} \right) = (l_1\Omega_1 + l_2\Omega_2)\frac{dF_0}{dE} \rightarrow l_3\Omega_{\mathrm{p}}\frac{dF_0}{dE}$$

because of the δ-function. Then the LBK torque is

$$\mathcal{T} = \sum_{l_1,l_2 = -\infty}^{\infty} \sum_{l_3 = 1}^{\infty} \mathcal{T}_{l_1 l_2 l_3}, \qquad \text{where} \qquad (25a)$$

$$\mathcal{T}_{l_1 l_2 l_3} = 16\pi^4\, l_3^2\, \Omega_{\mathrm{p}} \int d\boldsymbol{I}\, \frac{dF_0}{dE}$$
$$\times \delta(l_1\Omega_1 + l_2\Omega_2 - l_3\Omega_{\mathrm{p}})|\widetilde{\Phi}_{l_1 l_2 l_3}(\boldsymbol{I})|^2. \quad (25b)$$

Therefore, the torque due to each resonance, $\mathcal{T}_{l_1 l_2 l_3}$, has a sign that is opposite to Ω_{p}; the perturber always experiences a retarding torque.

3. Model of Dynamical Friction on a GC

The unperturbed galaxy is chosen to have an isochrone DF because it is a realistic representation of a stable spherical galaxy with isotropic velocity dispersion, with remarkably simple analytical representations of physical quantities (Hénon 1959a, 1959b, 1960; Binney & Tremaine 2008). The perturber is a GC on a circular orbit in the x–y plane, modeled as a Plummer sphere of small core radius. The rate of decay of the GC's orbital radius is determined by the back-reacting torque exerted by the galaxy.

3.1. Isochrone Galaxy Model

The gravitational potential of the isochrone model is

$$\Phi_0(r) = -\frac{GM}{b + \sqrt{b^2 + r^2}}, \quad (26)$$

where M is the total mass of the galaxy, and b is the core radius. The mass density profile that gives rise to this potential,

$$\rho_0(r) = \frac{1}{4\pi G}\,\boldsymbol{\nabla}^2\Phi_0(r)$$
$$= M\left[\frac{3(b^2 + r^2)(b + \sqrt{b^2 + r^2}) - r^2(b + 3\sqrt{b^2 + r^2})}{4\pi(b + \sqrt{b^2 + r^2})^3(b^2 + r^2)^{3/2}} \right]$$
$$(27)$$

---

[4] This is identical to Equation (66) of TW84, when $\widetilde{\Phi}_{l_1 l_2 l_3} \to \Psi_{l_1 l_2 l_3}/2$, to correspond to the differing conventions used in the definition of the Fourier coefficients of the perturbing potential.

is a decreasing function of r: the central density is $\rho_0(0) = 3M/16\pi b^3$ and $\rho_0(r) \to bM/2\pi r^4$ as $r \to \infty$. The stellar mass enclosed within a radius r is

$$M_0(r) = 4\pi \int_0^r dr'\, r'^2\, \rho_0(r')$$
$$= M\left[\frac{r^3}{(b + \sqrt{b^2 + r^2})^2 \sqrt{b^2 + r^2}} \right]. \quad (28)$$

A GC of mass M_p is on a circular orbit in the x–y plane of the galaxy. When the GC is at a radius r_p from the galactic center, its angular frequency of rotation is

$$\Omega_p(r_p) = \sqrt{\frac{G\,[M_0(r_p) + M_p\,]}{r_p^3}}. \quad (29)$$

As in Section 2.3, we use $\boldsymbol{r} = (r, \theta, \phi)$ for the position vector in the rotating frame with the origin at the center of the galaxy and $\boldsymbol{p} = (p_r, p_\theta, p_\phi)$ to denote its conjugate momentum. The orbital energy per unit mass is

$$H_0 = \frac{1}{2}\left(p_r^2 + \frac{p_\theta^2}{r^2} + \frac{p_\phi^2}{r^2 \sin^2\theta} \right) + \Phi_0(r). \quad (30)$$

The Jacobi Hamiltonian governing unperturbed dynamics in the rotating frame is

$$H_{J0} = H_0 - \Omega_p(r_p)p_\phi. \quad (31)$$

We now switch to the action-angle variables of Equation (13). Dropping all indices, we have

$$\text{Actions} = (I, L, L_z), \quad \text{where} \quad I = 2J_r + L; \quad (32a)$$

$$\text{Angles} = (w, g, h), \quad \text{where}$$

$$w = \frac{\Omega_r}{2}(t - t_p),$$

$$g = \chi + \left(\Omega_\psi - \frac{\Omega_r}{2} \right)(t - t_p),$$

$$h = \text{longitude of the ascending node.} \quad (32b)$$

The radial and angular frequencies are

$$\Omega_r(I, L) = \frac{8(GM)^2}{[I + \sqrt{I_b^2 + L^2}\,]^3},$$

$$\Omega_\psi(I, L) = \frac{\Omega_r}{2}\left(1 + \frac{L}{\sqrt{I_b^2 + L^2}} \right), \quad (33)$$

where $I_b = \sqrt{4GMb}\ = \text{constant}$. The orbital energy per unit mass, $H_0 = E$, is

$$E(I, L) = -\frac{2(GM)^2}{[I + \sqrt{I_b^2 + L^2}\,]^2}. \quad (34)$$

Hence, the Jacobi Hamiltonian governing dynamics in the rotating frame is a simple function of the three actions,

$$H_{J0}(I, L, L_z; r_p) = E(I, L) - \Omega_p(r_p)L_z, \quad (35)$$

where we have included the dependence on $r_p(t)$, the radius of the GC's circular orbit. This is an adiabatically varying function of time ("orbital decay") that is calculated self-consistently in Section 6. The three actions, (I, L, L_z), are

constants along an orbit. The unperturbed frequencies are

$$\Omega_w(I, L) = \frac{\partial H_{J0}}{\partial I} = \frac{4(GM)^2}{[I + \sqrt{I_b^2 + L^2}\,]^3}, \quad (36a)$$

$$\Omega_g(I, L) = \frac{\partial H_{J0}}{\partial L} = \frac{L}{\sqrt{I_b^2 + L^2}}\, \Omega_w(I, L), \quad (36b)$$

and

$$\Omega_h(I, L) = \frac{\partial H_{J0}}{\partial L_z} = -\,\Omega_p(r_p). \quad (36c)$$

The DF with isotropic velocity dispersion is

$$F_0(E) = \frac{M}{\sqrt{2}\,(2\pi)^3(GMb)^{3/2}}\frac{\sqrt{\mathcal{E}}}{[2(1 - \mathcal{E})]^4}$$
$$\times \Bigg[27 - 66\mathcal{E} + 320\mathcal{E}^2 - 240\mathcal{E}^3 + 64\mathcal{E}^4$$
$$+ 3(16\mathcal{E}^2 + 28\mathcal{E} - 9)\frac{\arcsin\sqrt{\mathcal{E}}}{\sqrt{\mathcal{E}(1 - \mathcal{E})}} \Bigg], \quad (37)$$

where $\mathcal{E} = -Eb/GM$ is a dimensionless measure of the binding energy, with $0 < \mathcal{E} \leqslant 1/2$. Here $F_0(E)$ is a decreasing function of E and hence has the desirable property of being linearly stable to perturbations.

3.1.1. Choice of Parameters

We now choose isochrone parameters, central density $\rho_0(0)$ and core radius b, such that they are broadly consistent with In11, whose simulation used a Burkert (1995) density profile for the galaxy,

$$\rho_B(r) = \frac{\rho_c r_c^3}{(r_c + r)(r_c^2 + r^2)}, \quad (38)$$

with core radius $r_c = 1000\,\text{pc}$ and central density $\rho_c = 0.1\,M_\odot\,\text{pc}^{-3}$. Here ρ_c was determined by requiring that the mass inside $300\,\text{pc}$ was about $10^7\,M_\odot$, consistent with observations of dwarf galaxies (Strigari et al. 2008). Setting the isochrone core radius $b = r_c = 1000\,\text{pc}$, we solve for $\rho_0(0)$ by setting $M_0(300\,\text{pc}) = 10^7\ M_\odot$ in Equation (28). This gives $\rho_0(0) = 0.096\ M_\odot\text{pc}^{-3}$, which is very close to ρ_c. So our isochrone model has the same core radius and central density as the Burkert profile in In11. We note that the total mass of the isochrone is $M = 1.6 \times 10^9\,M_\odot$, whereas the total mass in the Burkert profile is infinite because $\rho_B(r) \propto r^{-3}$ for $r \gg r_c$. But this large r behavior has no bearing on the core dynamics of interest to us. Indeed, it proves more useful—see Section 7—to define the "core" mass,

$$M_c = \frac{4\pi}{3}\rho_0(0)b^3 \simeq \frac{4\pi}{3}\rho_c r_c^3 \simeq 4 \times 10^8\,M_\odot, \quad (39)$$

which is the same for both galaxy profiles.

3.2. Expectation from the Chandrasekhar Formula

Before computing the orbital decay, $r_p(t)$, of a GC using the LBK torque, we need a benchmark in terms of what one may expect in an isochrone galaxy, according to the Chandrasekhar formula. Similar to In11, we assume that the GC has a mass
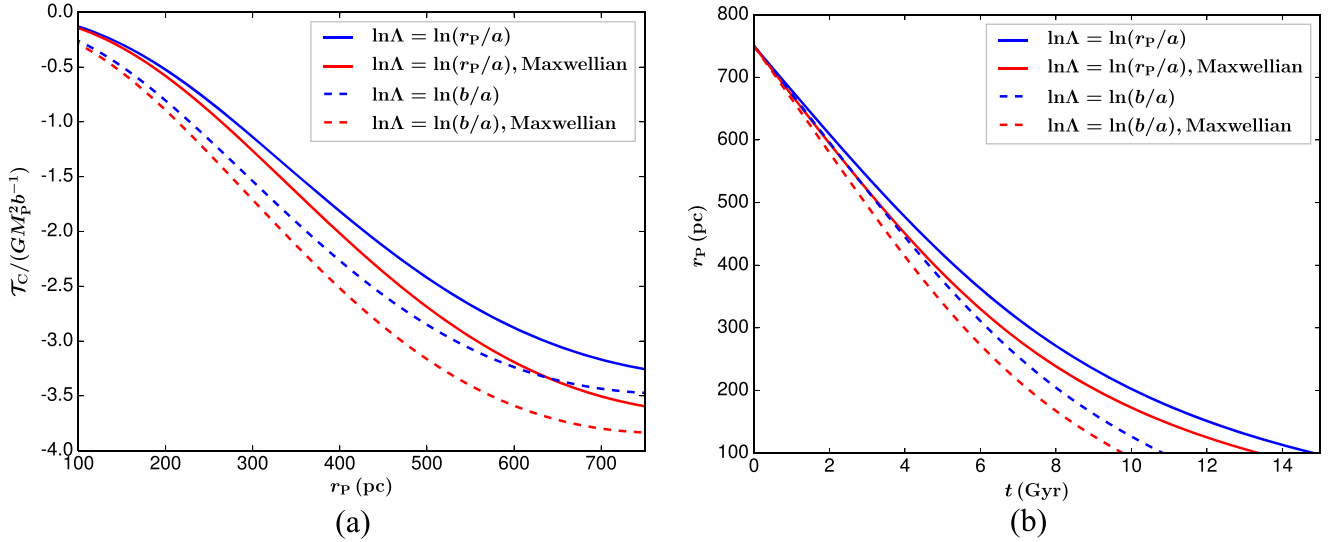
Figure 1. Torque profiles and orbital decay in the isochrone model according to the Chandrasekhar formula. Blue curves are for $\rho(r_{\rm P}; v < \Omega_{\rm p} r_{\rm p})$ determined by integrating the isochrone DF of Equation (37) over velocities. Red curves are for $\rho(r_{\rm P}; v < \Omega_{\rm p} r_{\rm p})$ determined by using the isochrone density profile of Equation (27) and a "local" Maxwellian distribution of velocities. Solid and dashed lines correspond to the two different choices of $\ln\Lambda$, as explained in the text.

$M_p = 2 \times 10^5 \, M_\odot$ and core radius $a = 10$ pc. Equation (1) implies that the rate of loss of the GC's orbital angular momentum is

$$M_{\rm p} \frac{d}{dt}(\Omega_{\rm p} r_{\rm p}^2) = \mathcal{T}_{\rm C}(r_{\rm p}), \qquad (40)$$

where

$$\mathcal{T}_{\rm C}(r_{\rm p}) = -4\pi G^2 M_{\rm p}^2 \ln\Lambda \, \rho(r_{\rm p}; v < \Omega_{\rm p} r_{\rm p}) \frac{1}{\Omega_{\rm p}^2 \, r_{\rm p}} \qquad (41)$$

is the Chandrasekhar torque. We need to determine the two quantities, $\ln\Lambda$ and $\rho(r_{\rm p}; v < \Omega_{\rm p} r_{\rm p})$. This is a "local" approximation, so some sense needs to be made of the Coulomb logarithm. The standard choice is discussed in Binney & Tremaine (2008), and modifications have been suggested. We consider two extreme choices that should act as upper and lower bounds on what can be expected. These are $\ln\Lambda = \ln(b/a) = 4.6$ and $\ln\Lambda = \ln(r_{\rm p}/a)$, which varies from 4.3 to 3.4 as $r_{\rm p}$ varies from 750 to 300 pc. The quantity $\rho(r_{\rm p}; v < \Omega_{\rm p} r_{\rm p})$ is the mass density at $r_{\rm p}$ of stars with speeds less than $\Omega_{\rm p} r_{\rm p}$. The direct way to calculate this is by integrating the isochrone DF of Equation (37) over the velocities. But it is also traditional (Binney & Tremaine 2008; In11) to simplify further by pushing the "local" nature of approximation in this manner: the DF is assumed to be the product of the galaxy's density profile (e.g., the isochrone $\rho_0(r)$ of Equation (27)) and a Maxwellian distribution of velocities with dispersion $\sigma(r)$ determined by the Jeans equations of hydrostatic equilibrium.

With two choices each for $\rho(r_{\rm p}; v < \Omega_{\rm p} r_{\rm p})$ and $\ln\Lambda$, we get four different functional forms for the Chandrasekhar torque; see Figure 1(a). Substituting these in Equation (40) and integrating with the initial condition, $r_{\rm p} = 750$ pc at $t = 0$, we obtain the orbital decay of $r_{\rm p}(t)$ for the four cases; see Figure 1(b). For 300 pc $< r_{\rm p} <$ 750 pc, the torques differ from each other by factors less than 1.5. The time for $r_{\rm p}$ to decay from 750 to 300 pc varies from 5.6 to 7.3 Gyr. After 10 Gyr, all models of the Chandrasekhar torque predict that the GC would be within 200 pc of the center.

3.3. LBK Torque

The LBK torque of Equations 25(a) and (b) is

$$\mathcal{T}(r_{\rm p}) = \sum_{n,\ell=-\infty}^{\infty} \sum_{m=1}^{\infty} \mathcal{T}_{n\ell m}(r_{\rm p}), \quad \text{where} \qquad (42a)$$

$$\mathcal{T}_{n\ell m}(r_{\rm p}) = 16\pi^4 \, m^2 \, \Omega_{\rm p} \int_0^\infty dI \int_0^I dL \, \frac{dF_0}{dE}$$
$$\times \, \delta(n\Omega_w + \ell\Omega_g - m\Omega_{\rm p}) \int_{-L}^{L} dL_z \, |\widetilde{\Phi}_{n\ell m}(I, L, L_z)|^2. \qquad (42b)$$

We need to compute $\widetilde{\Phi}_{n\ell m}(I, L, L_z)$ for a GC modeled as a rigid Plummer sphere of mass $M_{\rm p}$ and core radius $a = 10$ pc, as in In11. Its position vector with respect to the center of the galaxy, $\boldsymbol{r}_{\rm p}$, is quasi-stationary in the rotating frame. The perturbing potential experienced by a star at $\boldsymbol{r}$ is equal to the tidal potential due to the GC:[5]

$$\Phi_{\rm P} = \frac{-GM_p}{\sqrt{a^2 + |\boldsymbol{r} - \boldsymbol{r}_{\rm p}|^2}} + \frac{GM_p(\boldsymbol{r} \cdot \boldsymbol{r}_{\rm p})}{(a^2 + r_{\rm p}^2)^{3/2}}. \qquad (43)$$

The function $\Phi_{\rm p}(w, g, h; I, L, L_z)$ can be obtained by writing $\boldsymbol{r}$ in terms of the action-angle variables of Equation (32). The orbital plane is determined by its constant inclination, $i = \arccos(L_z/L)$, and the longitude of the ascending node, h. The radius (r) and angle in the orbital plane (ψ) can both be expressed in terms of $\{w, g, h; I, L, L_z\}$ by first defining three quantities (see Binney & Tremaine 2008, Section 3.5.2):

$$c(I, L) = -\frac{GM}{2E} - b, \qquad (44a)$$

$$e^2(I, L) = 1 - \frac{L^2}{GMc}\left(1 + \frac{b}{c}\right), \qquad (44b)$$

---

[5] In the terminology of planetary dynamics, $\Phi_{\rm p}$ is the "disturbing function," which is the sum of the "direct" and "indirect" terms (Murray & Dermott 1999).

and

$$w = \frac{1}{2}\left(\eta - \frac{ec}{c+b}\sin\eta\right). \tag{44c}$$

Here $c(I, L)$ is a length scale, $e(I, L)$ is an "eccentricity," and η is an "eccentric anomaly." Then,

$$r^2 = [b + c(1 - e\cos\eta)]^2 - b^2 \tag{45a}$$

and

$$\psi = g + \arctan\left(\sqrt{\frac{1+e}{1-e}}\,\tan(\eta/2)\right) + \frac{L}{\sqrt{I_b^2 + L^2}}$$
$$\times\left\{\arctan\left[\sqrt{\frac{1+e+2b/c}{1-e+2b/c}}\,\tan(\eta/2)\right] - w\right\} \tag{45b}$$

give (r, ψ) in terms of (I, L, η, g), and Equation 44(c) can be used to express η in terms of (w, I, L) as required. The Fourier coefficients of Φ_p of Equation (43) can then be computed as

$$\widetilde{\Phi}_{n\ell m}(I, L, L_z) = \oint \frac{dw}{2\pi}\frac{dg}{2\pi}\frac{dh}{2\pi}\,\Phi_p(w, g, h; I, L, L_z)$$
$$\times \exp\{-i(nw + \ell g + mh)\}. \tag{46}$$

4. Resonances in the Isochrone Core

4.1. Unperturbed Orbits

The (n, ℓ, m) resonance,

$$n\,\Omega_w(I, L) + \ell\,\Omega_g(I, L) - m\,\Omega_p(r_p) = 0, \tag{47}$$

is a curve in the (I, L) plane. Resonant stars with orbital sizes comparable to the core radius have Ω_g comparable to Ω_w. This implies that solutions of Equations (47) are possible for numerous triplets, $(n, \ell, m > 0)$. So there are many resonances of comparable strengths in operation. TW84 argued that, in the limit that the resonances form a continuum, the LBK torque should reduce to the Chandrasekhar torque. Here $\ln\Lambda = \ln(b_{max}/b_{min})$, where b_{max} and b_{min} are the maximum and minimum impact parameters of the encounter between the GC and stars. We set $b_{max} = r_p$, the orbital radius of the GC (see Binney & Tremaine 2008), and $b_{min} = a = 10$ pc, to match the In11 value of the GC's core radius. Then, $\ln\Lambda = \ln(r_p/a)$ varies from 4.3 at $r_p = 750$ pc to 3.4 at $r_p = 300$ pc, which is approximately consistent with the constant best-fit value of 3.72 used by In11.

When $r_p = 300$ pc, the Chandrasekhar formula is still approximately valid with $b_{max} = 300$ pc, as we confirm in Section 6. For $r_p < 300$ pc, the rate of orbital decay slows down dramatically in In11. There is a significant departure from the predictions of the Chandrasekhar torque until it breaks down completely when the cluster stalls at a mean orbital radius of about 225 pc, being affected by stars with orbital radii ≈ 400 pc (i.e., stars with $b_{max} \approx 200$ pc). Hence, in order to describe dynamical friction for $r_p \leqslant 300$ pc, we can focus attention on stars whose orbital radii $\lesssim 600$ pc. These stars oscillate well within the core radius of the galaxy, $b = 1000$ pc, so $I \ll I_b$ (we always have $0 \leqslant L \leqslant I$). Then,

Equations 44(a)–(c) reduce to

$$c \simeq 2\left(\frac{I}{I_b}\right)b, \qquad e^2 \simeq 1 - \frac{L^2}{I^2}, \qquad w \simeq \eta/2. \tag{48}$$

Also, Equations 45(a) and (b) now simplify,

$$r^2 \simeq \frac{I}{\Omega_b}[1 - e\cos(2w)], \tag{49a}$$

$$\psi \simeq g + \arctan\left(\sqrt{\frac{1+e}{1-e}}\,\tan w\right), \tag{49b}$$

where

$$\Omega_b = \frac{1}{2}\sqrt{\frac{GM}{b^3}} = \sqrt{\frac{4\pi}{3}G\rho_0(0)} \tag{50}$$

depends only on the central density. The mean-squared orbital radius is $r_{rms}^2 = I/\Omega_b$. We consider the response of stars with $r_{rms} \leqslant r_{max} \simeq 632$ pc. This provides a dynamically useful definition of "core stars" as those whose action variable $I \leqslant I_{max} = \Omega_b\,r_{max}^2$. We define

$$\varepsilon = \frac{I_{max}}{I_b} = \frac{1}{4}\left(\frac{r_{max}}{b}\right)^2 = \frac{1}{10}. \tag{51}$$

Because $I, L < I_{max}$, both I/I_b and L/I_b are smaller than ε in the core. So ε is a natural small parameter of the problem. To first order in ε, the unperturbed frequencies of Equations 36(a) and (c) reduce to

$$\Omega_w(I) \simeq \Omega_b\left(1 - 3\frac{I}{I_b}\right), \qquad \Omega_g(L) \simeq \Omega_b\left(\frac{L}{I_b}\right). \tag{52}$$

The maximum error in this is $O(\varepsilon^2) = 1\%$.

A core star moves on an ellipse with orbital frequency $\Omega_w(I)$, while the apsides of the ellipse precess forward with frequency $\Omega_g(L)$. The frequencies are not constants but depend on (I, L).[6] The orbital plane maintains a constant inclination $i = \arccos(L_z/L)$ with its line of nodes precessing with frequency $-\Omega_p(r_p)$ (because the orbit is viewed in the rotating frame).

As I varies from 0 to I_{max}, Ω_w decreases from Ω_b to $(1-3\varepsilon)\Omega_b$, so Ω_b is the central orbital frequency with a corresponding time period $T_b = 2\pi/\Omega_b \simeq 1.48 \times 10^8$ yr. As L varies from 0 to its maximum possible value of I_{max}, Ω_g increases from 0 to $\varepsilon\Omega_b$. Let $T_w = 2\pi/\Omega_w$, $T_g = 2\pi/\Omega_g$ be the orbital and apse precession time periods, respectively. Then we have $(1-3\varepsilon)^{-1}\,T_b \geqslant T_w \geqslant T_b$, so that $T_w \sim$ few $\times 10^8$ yr and $T_g \geqslant \varepsilon^{-1}\,T_b = 1.48 \times 10^9$ yr. The nodal regression period, $T_h = 2\pi/\Omega_p$, depends on r_p. In order to follow the In11 simulation, it will suffice to look at 150 pc $< r_p <$ 300 pc, in which range we have $\Omega_p \simeq \Omega_b$, as can be verified using Equation (29). Hence, $T_h \simeq T_b \simeq 1.48 \times 10^8$ yr.

Below, we study resonances involving the three time periods, T_w, T_g, and T_h. Of these, T_w and T_h are of comparable magnitudes, but T_g is more than 10 times longer than these. Hence, we may expect the dominant resonances to involve close cancellation between T_w and T_h, corresponding to resonant stars that nearly corotate with the GC, as discussed in Section 4.4.

---

[6] In an exactly constant density core, we would have $\Omega_w = \Omega_b =$ constant and $\Omega_g = 0$. But this exactly harmonic limit is pathological, as discussed in Sections 1 and 7.
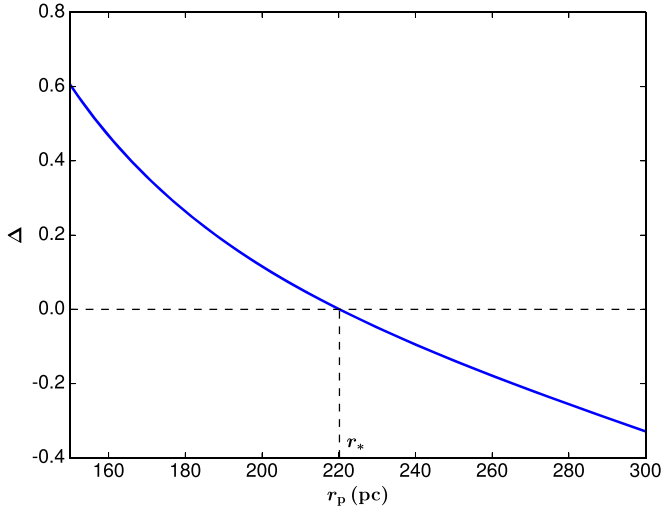
Figure 2. Normalized fractional frequency difference as a function of the GC's orbital radius.

Figure 3. Shown is $A(X, Y)$ in the unit triangle.

4.2. Resonance Filtering Radius r_*

The core resonance conditions are obtained by substituting Equation (52) in Equation (47):

$$n \, \Omega_b \left(1 - 3 \, \frac{I}{I_b} \right) + \ell \, \Omega_b \left(\frac{L}{I_b} \right) - m \, \Omega_p(r_p) = 0. \qquad (53)$$

For any given $(n, \ell, m > 0; r_p)$, this gives a straight line in the (I, L)-plane. However, we are interested in the response of core stars whose $I \leqslant I_{\max}$. Therefore, core resonances are restricted to those $(n, \ell, m > 0; r_p)$ such that the resonant line passes through the triangle, $0 \leqslant (L/I_b) \leqslant (I/I_b) \leqslant \varepsilon$, in the (I, L)-plane. Since $\Omega_p \simeq \Omega_b$, we write $\Omega_p = \Omega_b [1 + \varepsilon \Delta(r_p)]$. The normalized fractional frequency difference,

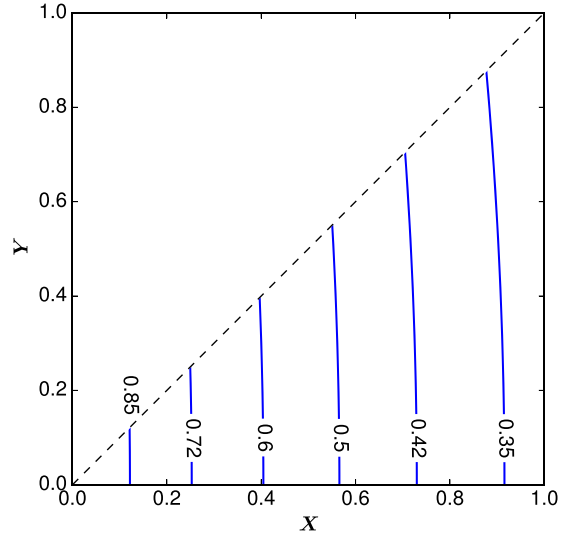$$\Delta(r_p) = \frac{\Omega_p(r_p) - \Omega_b}{\varepsilon \Omega_b}, \qquad (54)$$

determines which resonances are allowed at any given r_p. It can be computed using Equation (29) and is displayed in Figure 2. Here $\Delta(r_p)$ is a smooth, order-unity, decreasing function of r_p, varying from about $+0.6$ at $r_p = 150 \, \mathrm{pc}$ to -0.33 at $r_p = 300 \, \mathrm{pc}$ and passing through zero at $r_p = r_* \simeq 220 \, \mathrm{pc}$.

The radius r_* has a simple interpretation in terms of the galaxy's core density profile. We recall that r_* is defined as the radius at which $\Omega_p(r_p) = \Omega_b$, where $\Omega_p(r_p)$ is the GC's circular orbital frequency and Ω_b is the orbital frequency of stars at the very center of the galaxy. Rearranging Equations (29) and (50), we obtain[7]

$$\frac{4\pi}{3} \rho(0) r_*^3 - M(r_*) = M_p. \qquad (55)$$

The left side of Equation (55) is the difference in the mass enclosed within r_* ("mass deficit") between a hypothetical constant density core and that given by the mass profile of the galaxy. Therefore, r_* is the radius at which the galactic mass deficit is equal to the mass of the GC.

The mass deficit vanishes for a constant density core, $\rho(r) = \rho(0) = \text{constant}$, so Equation (55) cannot be satisfied for nonzero M_p, emphasizing the importance of allowing for core density variation. It is precisely the deviation from a constant density core that enables resonances and associated torques.

Formulae for r_* for the isochrone and Burkert density profiles are given in Equations 81(a) and (b) of Section 7. In Section 5, we study in detail the role of r_* as a "filtering" radius for many low-order resonances, which is applied in Section 6 to the orbital decay of the GC.

4.3. Torques in Dimensionless Variables

We now express the resonant torques of Equation 42(b) using the dimensionless variables (X, Y, Z),

$$X = \frac{I}{I_{\max}}, \qquad Y = \frac{L}{I_{\max}}, \qquad Z = \frac{L_z}{I_{\max}}, \qquad (56)$$

instead of (I, L, L_z). The domain of these is restricted to the three-dimensional wedge, $0 \leqslant Y \leqslant X \leqslant 1$, with $-Y \leqslant Z \leqslant Y$. Equation (37) for the isochrone DF can be written as

$$\frac{dF_0}{dE} = -19.05 \, \frac{b}{G I_b^3} A(X, Y), \qquad (57)$$

where $A(X, Y)$ is a dimensionless positive function with $A(0, 0) = 1$. From Figure 3, it can be seen that $A(X, Y)$ is weakly dependent on Y. We also rescale and define the dimensionless Fourier coefficients,

$$\Phi_{n\ell m}(X, Y, Z) = \frac{(a^2 + r_p^2)^{1/2}}{G M_p} \widetilde{\Phi}_{n\ell m}(I, L, L_z). \qquad (58)$$

The torques depend on

$$P_{n\ell m}(X, Y) = \int_{-Y}^{Y} dZ \, |\Phi_{n\ell m}(X, Y, Z)|^2, \qquad (59)$$

---

[7] The subscript "0" has been dropped for the central density and mass profile of the galaxy to indicate that Equation (55) is valid for any decreasing density profile, $\rho(r)$, with a finite central density, $\rho(0)$, and not just the isochrone.

which is a measure of the distribution within the unit triangle of the "power" in the $(n\ell m)$ Fourier component. Using Equations (53), (57), and (59) in Equation 42(b), the resonant torque is

$$\mathcal{T}_{n\ell m}(r_p) = -305\,\pi^4\varepsilon^2\frac{GM_p^2\,b\,[1+\varepsilon\Delta(r_p)]}{a^2+r_p^2}\,\mathcal{F}_{n\ell m}(r_p), \quad (60)$$

where

$$\mathcal{F}_{n\ell m}(r_p) = m^2\int_0^1 dX\int_0^X dY\,A(X,Y)P_{n\ell m}(X,Y)$$
$$\times\,\delta(\varepsilon^{-1}(n-m)-3nX+\ell Y-m\Delta) \quad (61)$$

is a dimensionless positive factor that measures the strength of a resonance.

4.4. Types of Resonances

The resonance condition of Equation (53) can be rewritten in dimensionless form as

$$\frac{(n-m)}{\varepsilon}+\{-3nX+\ell Y-m\Delta(r_p)\}=0, \quad (62)$$

where we note that it is independent of Z. We recall that $m=1,2,3$, etc., and only one of (n,ℓ) can be zero. Given r_p, for a triplet $(n,\ell,m>0)$ to be a core resonance, the straight line of Equation (62) must pass through the unit triangle, $0\leqslant Y\leqslant X\leqslant 1$. The magnitudes of the three terms inside the curly brackets of the resonance condition, Equation (62), are of order $3n$, ℓ, and m, respectively. For the resonance condition to be satisfied, these three terms together must cancel $\varepsilon^{-1}(n-m)=10(n-m)$.

Of particular importance are resonances with small integers, $(n,\ell,m>0)$. This is because the resonance strength, $\mathcal{F}_{n\ell m}$, of Equation (61) depends on $P_{n\ell m}$, which diminishes rapidly for larger $(n,\ell,m>0)$. Hence, it is natural to distinguish between the two main types of core resonances accordingly as $n=m$ or $n\neq m$.

1. Corotating resonances: $n=m>0$. Then, Equation (62) reduces to

$$-3mX+\ell Y-m\Delta(r_p)=0. \quad (63)$$

As this equation can be satisfied by many low integers ℓ and $m>0$, we expect corotating resonances to exert significant torques. A physical picture of the orbit of a corotating resonant star can be obtained by setting $n=m$ in Equation (47), which is the primitive form of the resonance condition:

$$m[\Omega_w(I,L)-\Omega_p]=-\ell\,\Omega_g(I,L).$$

Because $(\Omega_w,\Omega_g,\Omega_p,m)$ are all positive quantities with $\Omega_w,\Omega_p\gg\Omega_g$, we must have $\Omega_w\simeq\Omega_p$, with the small difference between them resonating with Ω_g, the small apse precession rate. So, a resonant star nearly corotates with the GC, trailing or leading it slightly, depending on the sign of ℓ. Thus, we have the two families of corotating resonances:

trailing resonances $\ell>0$, so $\Omega_w<\Omega_p$ and the star trails the GC in its orbit; and
leading resonances $\ell\leqslant 0$, so $\Omega_w\geqslant\Omega_p$ and the star leads the GC in its orbit.

2. Non-corotating resonances: $n\neq m$. In this case, Ω_w can differ from Ω_p considerably. The resonance condition of

Equation (62) retains its general form. The first term is now nonzero, with magnitude $\varepsilon^{-1}|n-m|=\varepsilon^{-1},2\varepsilon^{-1},3\varepsilon^{-1}$, etc. $=$ 10, 20, 30, etc. Each of the three terms in the curly brackets can be as large only if either $|n|\geqslant 4,7,10$, etc. or $|\ell|,m\geqslant$ 10, 20, 30, etc. Therefore, these are all higher-order resonances whose torques will be much weaker than corotating torques.

5. Corotating Torques in the Core

Here we study trailing and leading corotating resonances and compute the associated torques as functions of the GC's orbital radius for $150\,\text{pc}\leqslant r_p\leqslant 300\,\text{pc}$. We follow the progressive disappearances of resonances as r_p decreases and see the role of $r_*\simeq 220\,\text{pc}$ as a characteristic "filtering radius."

The numerically intensive part of calculating the $\mathcal{F}_{m\ell m}(r_p)$ is in the evaluation of the Fourier coefficients, $\widetilde{\Phi}_{n\ell m}(I,L,L_z)$, defined in Equation (46): for each (I,L,L_z), we need to do a triple integral over the angles (w,g,h). Computation is expedited by noting that, by suitable transformation to new angle variables, one of the integrals can be evaluated analytically in terms of elliptic integrals, as given in the Appendix. The remaining two angle integrals are then computed numerically. Once we have $\mathcal{F}_{m\ell m}(r_p)$, it can be substituted in Equation (60) to get the resonant torque, $\mathcal{T}_{m\ell m}(r_p)$. Then, the net trailing and leading torque profiles are

$$\mathcal{T}_{\text{trail}}(r_p)=\sum_{m>0}\sum_{\ell>0}\mathcal{T}_{m\ell m}(r_p), \quad (64a)$$

$$\mathcal{T}_{\text{lead}}(r_p)=\sum_{m>0}\sum_{\ell\leqslant 0}\mathcal{T}_{m\ell m}(r_p), \quad (64b)$$

where the sums are over those (m,ℓ) for which, at a given r_p, the resonant line lies within the unit triangle in (X,Y)-space. We discuss these in Sections 5.1 and 5.2 for trailing and leading resonances, respectively. Each has two subcases according to whether the GC is outside or inside r_*.

5.1. Trailing Corotating Torques

Since $\ell>0$, Equation (63) implies that resonant lines have positive slopes in the (X,Y)-plane.

5.1.1. GC Outside r_*

When $r_*\leqslant r_p<300\,\text{pc}$, we have $-0.33<\Delta\leqslant 0$. Equation (63) gives

$$X=X_r(Y;m,\ell,r_p)\overset{\text{def}}{=}\frac{|\Delta|}{3}+\frac{\ell}{3m}Y \quad (65)$$

as the resonant line, which intersects two of the three edges of the unit triangle. The line passes through the $Y=0$ edge at $X_1=|\Delta|/3$. The second point lies on the edge $Y=X$ for $\ell<(3-|\Delta|)m$ and on the edge $X=1$ for $\ell\geqslant(3-|\Delta|)m$. The torques behave differently, as discussed below.

Low-ℓ resonances, $\ell<(3-|\Delta|)m$. When $r_p=300\,\text{pc}$, we have $|\Delta|=0.33$, so $\ell<2.67m$ are the only integer values of ℓ that are allowed. We list some of the low-integer (m,ℓ) values
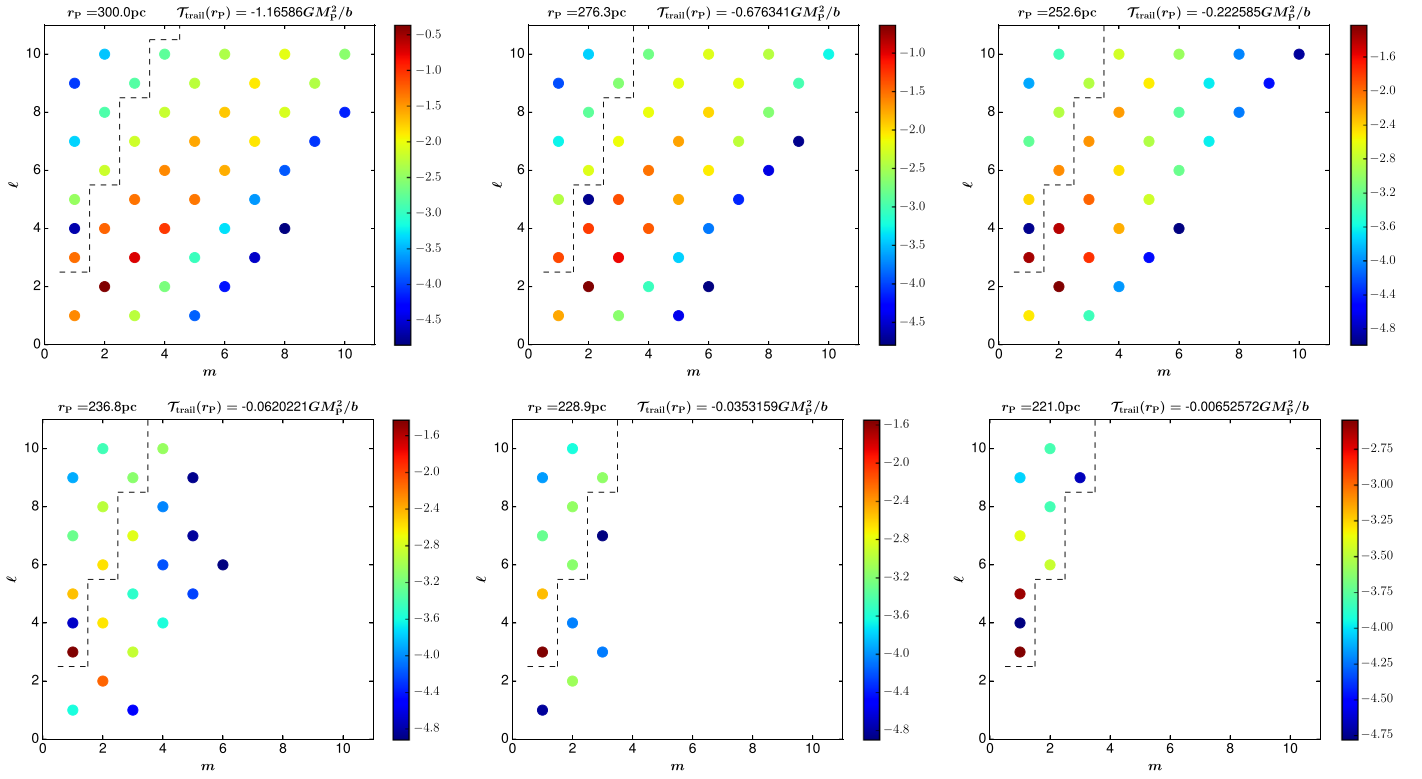
Figure 4. Trailing corotating resonances and torques for the GC outside r_* for six different $r_{\rm p} > r_*$. All $m, \ell \geqslant 1$ are allowed, but only resonances whose $|\mathcal{T}_{m\ell m}| > 10^{-5}(GM_{\rm p}^2 b^{-1})$ are displayed. The color scale refers to $\log_{10}[|\mathcal{T}_{m\ell m}|/(GM_{\rm p}^2 b^{-1})]$. The dashed lines separate low $\ell < (3 - |\Delta|)m$ from high $\ell \geqslant (3 - |\Delta|)m$ resonances.

that are allowed:

$$
\begin{array}{llll}
(1, 1) & (1, 2) & & \\
(2, 1) & (2, 2) & \ldots & (2, 5) \\
(3, 1) & (3, 2) & \ldots & (3, 8) \\
(4, 1) & (4, 2) & \ldots & (4, 10) \\
(5, 1) & (5, 2) & \ldots & (5, 13) \\
\ldots & \ldots & \ldots & \ldots .
\end{array} \tag{66}
$$

As $r_{\rm p}$ decreases, $|\Delta|$ also decreases, so the range of allowed ℓ increases. But this has only a modest effect for small m. The resonance strength factor of Equation (61) is

$$
\mathcal{F}_{m\ell m}(r_{\rm p}) = \frac{m}{3} \int_0^{Y_a} dY\, A(X_{\rm r}, Y) P_{m\ell m}(X_{\rm r}, Y), \tag{67}
$$

where $Y_a = m|\Delta|/(3\,m - \ell)$. Since the upper limit of integration, $Y_a \propto |\Delta| \to 0$ as $r_{\rm p} \to r_*$, all $\mathcal{F}_{m\ell m}(r_*) = 0$.

High-ℓ resonances, $\ell \geqslant (3 - |\Delta|)m$. When $r_{\rm p} = 300$ pc, we have $|\Delta| = 0.33$, so $\ell \geqslant 2.67m$ are the only integer values of ℓ that are allowed. The list of allowed (m, l) values is complementary to the list in Equation (66):

$$
\begin{array}{llll}
(1, 3) & (1, 4) & \ldots & \\
(2, 6) & (2, 7) & \ldots & \\
(3, 9) & (3, 10) & \ldots & \\
(4, 11) & (4, 12) & \ldots & \\
(5, 14) & (5, 15) & \ldots & \\
\ldots & \ldots & \ldots .
\end{array} \tag{68}
$$

As $r_{\rm p}$ decreases, $|\Delta|$ also decreases, and the range of allowed ℓ decreases. Again, this has only a modest effect for small m. The

range in ℓ is narrowest when $r_{\rm p} = r_*$ for which $|\Delta| = 0$; then $\ell \geqslant 3m$, and the list of allowed (m, ℓ) shrinks to

$$
\begin{array}{lll}
(1, 3) & (1, 4) & \ldots \\
(2, 6) & (2, 7) & \ldots \\
(3, 9) & (3, 10) & \ldots \\
(4, 12) & (4, 13) & \ldots \\
(5, 15) & (5, 16) & \ldots \\
\ldots & \ldots & \ldots .
\end{array} \tag{69}
$$

The allowed $m = 1, 2, 3$ resonances remain unaltered, but $(4, 11)$, $(5, 14)$, etc. have dropped out. The resonance strength factor of Equation (61) is

$$
\mathcal{F}_{m\ell m}(r_{\rm p}) = \frac{m}{3} \int_0^{Y_b} dY\, A(X_{\rm r}, Y) P_{m\ell m}(X_{\rm r}, Y), \tag{70}
$$

where $Y_b = (3 - |\Delta|)m/\ell$. At $r_{\rm p} = r_*$, we have $\ell \geqslant 3m$, $X_{\rm r} = (\ell/3m)Y$, and $Y_b = 3\,m/\ell$. It is important to note that $\mathcal{F}_{m\ell m}(r_*) \neq 0$, which is different from Equation (67) of the low-ℓ case.

The $\mathcal{F}_{m\ell m}(r_{\rm p})$ of Equations (67) and (70) were computed numerically, as discussed at the beginning of Section 5, for all 100 resonances with $1 \leqslant m, \ell \leqslant 10$. Substituting these in Equation (60), we obtained the corresponding $\mathcal{T}_{m\ell m}(r_{\rm p})$. The six panels of Figure 4 track trailing resonances with $|\mathcal{T}_{m\ell m}(r_{\rm p})| > 10^{-5}(GM_{\rm p}^2/b)$ for $r_* \leqslant r_{\rm p} \leqslant 300$ pc. Then, $\mathcal{T}_{\rm trail}(r_{\rm p})$ was calculated by summing over the $\mathcal{T}_{m\ell m}(r_{\rm p})$, as given in Equation 64(a). A striking feature evident in the figures is the progressive loss of resonances and torque strengths as $r_{\rm p}$ decreases.
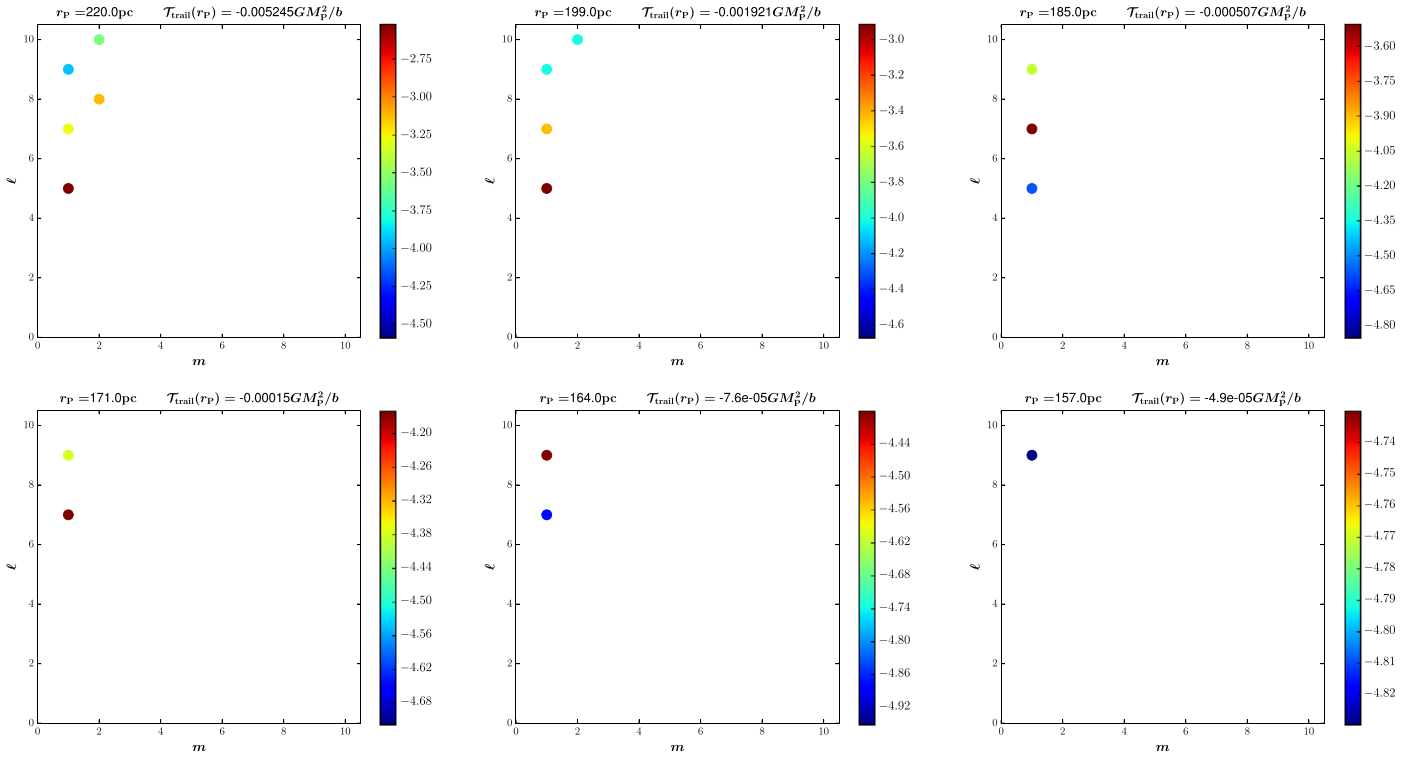
Figure 5. Trailing corotating resonances and torques for the GC inside r_* for six different $r_{\rm p} < r_*$. All $m \geqslant 1$ and $\ell > (3 + \Delta)m$ are allowed, but only resonances whose $|\mathcal{T}_{m\ell m}| > 10^{-5}(GM_{\rm p}^2 b^{-1})$ are displayed.

1. At $r_{\rm p} = 300$ pc, there are 43 resonances, with $10^{-5}(GM_{\rm p}^2/b) < |\mathcal{T}_{m\ell m}| \lesssim 10^{-0.36}(GM_{\rm p}^2/b)$. Of these, 34 are low-$\ell$ resonances and nine are high-ℓ resonances. The strongest torque comes from the (2, 2) resonance. The net torque due to all the resonances is $\mathcal{T}_{\rm trail} \simeq -1.17(GM_{\rm p}^2/b)$.
2. At $r_{\rm p} = 236.8$ pc, there are 24 resonances, with $10^{-5}(GM_{\rm p}^2/b) < |\mathcal{T}_{m\ell m}| \lesssim 10^{-1.4}(GM_{\rm p}^2/b)$. Of these, 15 are low-$\ell$ resonances and nine are the same high-ℓ resonances. The strongest torque comes from the (1, 3) resonance. The net torque due to all the resonances is $\mathcal{T}_{\rm trail} \simeq -6 \times 10^{-2}(GM_{\rm p}^2/b)$.
3. At $r_{\rm p} = 221$ pc, there are no low-ℓ resonances of any strength to speak of. Nine high-ℓ resonances survive, with $10^{-5}(GM_{\rm p}^2/b) < |\mathcal{T}_{m\ell m}| \lesssim 10^{-2.5}(GM_{\rm p}^2/b)$. The strongest torque still comes from the (1, 3) resonance. The net torque due to all the resonances is $\mathcal{T}_{\rm trail} \simeq -7 \times 10^{-3}(GM_{\rm p}^2/b)$.

The torque profile, $\mathcal{T}_{\rm trail}(r_{\rm p})$, is given in Figure 7(b) and discussed in Section 6.

5.1.2. GC Inside r_*

When 150 pc $< r_{\rm p} < r_*$, we have $0 < \Delta \leqslant 0.6$. Equation (63) gives

$$Y = Y_{\rm r}(X; m, \ell, r_{\rm p}) \overset{\rm def}{=} \frac{m}{\ell}\Delta + \frac{3m}{\ell}X \qquad (71)$$

as the resonant line. This lies in the unit triangle only when $\ell > (3 + \Delta)m$. It intersects the $X = Y$ edge at $X_1 = m\Delta/(\ell - 3m)$ and the $X = 1$ edge at $Y_2 = (3 + \Delta)m/\ell$.

For $r_{\rm p} \simeq r_*$, we have Δ small but positive. The list of allowed (m, ℓ) values is

$$
\begin{array}{cccc}
(1, 4) & (1, 5) & \dots & \\
(2, 7) & (2, 8) & \dots & \\
(3, 10) & (3, 11) & \dots & \\
(4, 13) & (4, 14) & \dots & \\
(5, 16) & (5, 17) & \dots & \\
\dots & \dots & \dots. & \qquad (72)
\end{array}
$$

This must be compared with the list in Equation (69) of high-ℓ resonances that survive at $r_{\rm p} = r_*$. We notice the absence of the $l = 3m$ resonances, so (1, 3), (2, 6), etc. have dropped out just inside r_*. As $r_{\rm p}$ decreases, Δ increases more steeply, leading to increased loss of the lower of these high-ℓ resonances. We calculated

$$\mathcal{F}_{m\ell m}(r_{\rm p}) = \frac{m^2}{\ell} \int_{X_1}^{1} dX\, A(X, Y_{\rm r}) P_{m\ell m}(X, Y_{\rm r}) \qquad (73)$$

for all 225 resonances with $1 \leqslant m, \ell \leqslant 15$. Substituting these in Equation (60), we obtained the corresponding $\mathcal{T}_{m\ell m}(r_{\rm p})$. The six panels of Figure 5 track the trailing (high-ℓ) resonances with $|\mathcal{T}_{m\ell m}(r_{\rm p})| > 10^{-5}(GM_{\rm p}^2/b)$ for 150 pc $\leqslant r_{\rm p} < r_*$. Then, $\mathcal{T}_{\rm trail}(r_{\rm p})$ was calculated by summing over $\mathcal{T}_{m\ell m}(r_{\rm p})$, as given in Equation 64(a). This set of figures should be seen as a continuation of the bottom right panel of Figure 4. High-ℓ resonances exist inside r_*, and there is increased loss of both resonances and torque strengths as $r_{\rm p}$ decreases.

1. At $r_{\rm p} = 220$ pc, which is just inside r_*, there are just five resonances with $10^{-5}(GM_{\rm p}^2/b) < |\mathcal{T}_{m\ell m}| \lesssim 10^{-2.5}(GM_{\rm p}^2/b)$. The strongest torque comes from the (1, 5) resonance. The
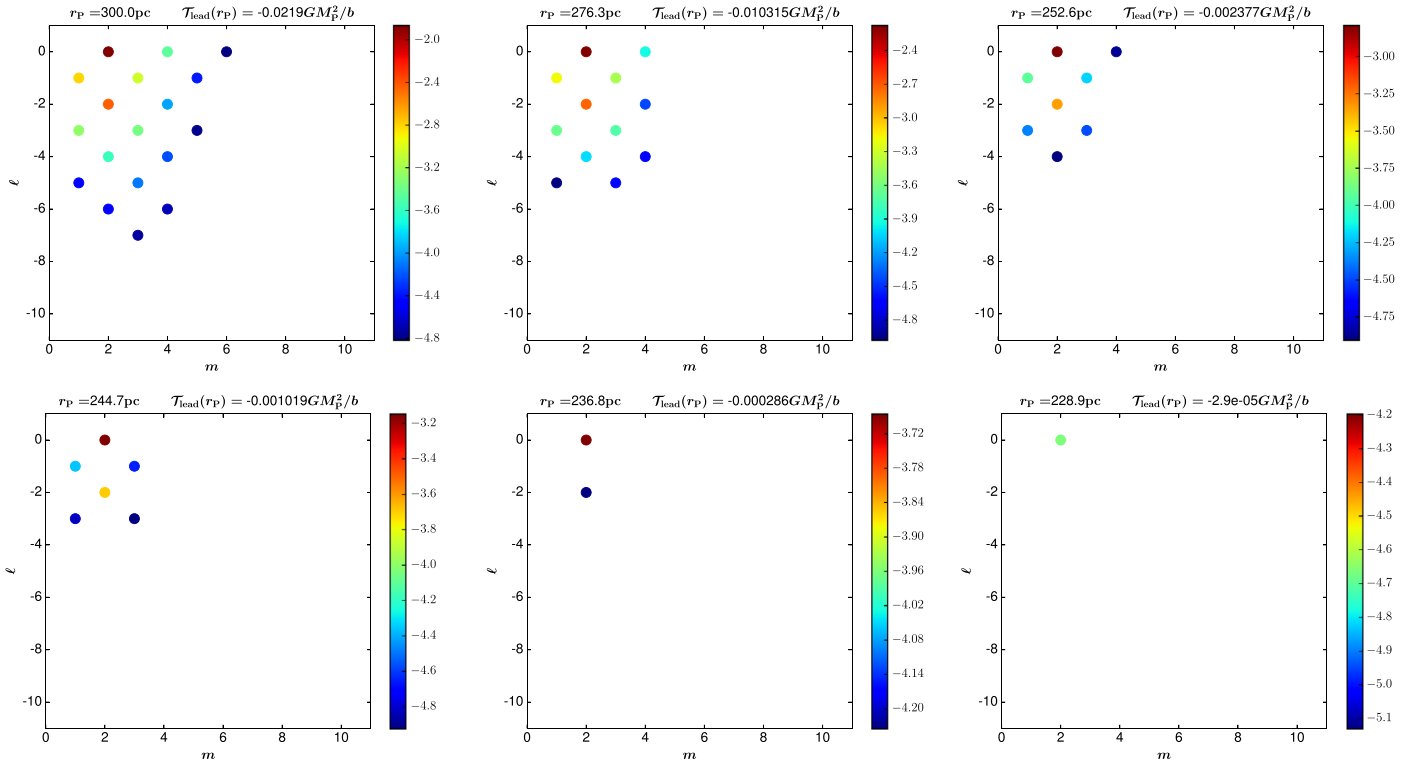
Figure 6. Leading corotating resonances and torques for the GC outside r_* for six different $r_p > r_*$. All $m \geqslant 1$ and $\ell \leqslant 0$ are allowed, but only resonances whose $|\mathcal{T}_{m\ell m}| > 10^{-5}(GM_p^2 b^{-1})$ are displayed.

net torque due to all resonances is $\mathcal{T}_{\mathrm{trail}} \simeq -5 \times 10^{-3}$ (GM_p^2/b).

2. At $r_p = 185$ pc, there are only three resonances with $10^{-5}(GM_p^2/b) < |\mathcal{T}_{m\ell m}| \lesssim 10^{-3.5}(GM_p^2/b)$. The strongest torque now comes from the $(1, 7)$ resonance. The net torque due to all resonances is $\mathcal{T}_{\mathrm{trail}} \simeq -5 \times 10^{-4}(GM_p^2/b)$.

3. At $r_p = 157$ pc, there is just one resonance left, $(1, 9)$, with $|\mathcal{T}_{m\ell m}| > 10^{-5}(GM_p^2/b)$. The net torque due to this, together with contributions from weaker resonances, is $\mathcal{T}_{\mathrm{trail}} \simeq -5 \times 10^{-5}(GM_p^2/b)$.

The torque profile, $\mathcal{T}_{\mathrm{trail}}(r_p)$, is given in Figure 7(a) and discussed in Section 6.

5.2. Leading Corotating Torques

When $\ell \leqslant 0$, the resonance condition of Equation (63) is

$$3mX + |\ell|Y + m\Delta(r_p) = 0. \tag{74}$$

Resonant lines have negative slopes in the (X, Y)-plane.

5.2.1. GC Outside r_*

When $r_* \leqslant r_p < 300$ pc, we have $-0.33 < \Delta \leqslant 0$, and Equation (74) gives

$$X = X_r(Y; m, \ell, r_p) \stackrel{\text{def}}{=} \frac{|\Delta|}{3} - \frac{|\ell|}{3m}Y \tag{75}$$

as the resonant line, which connects the points $(X_1, Y_1 = X_1)$ and $(X_2, 0)$, where

$$X_1 = \frac{|\Delta|}{3}\left(1 + \frac{|\ell|}{3m}\right)^{-1}, \qquad X_2 = \frac{|\Delta|}{3}. \tag{76}$$
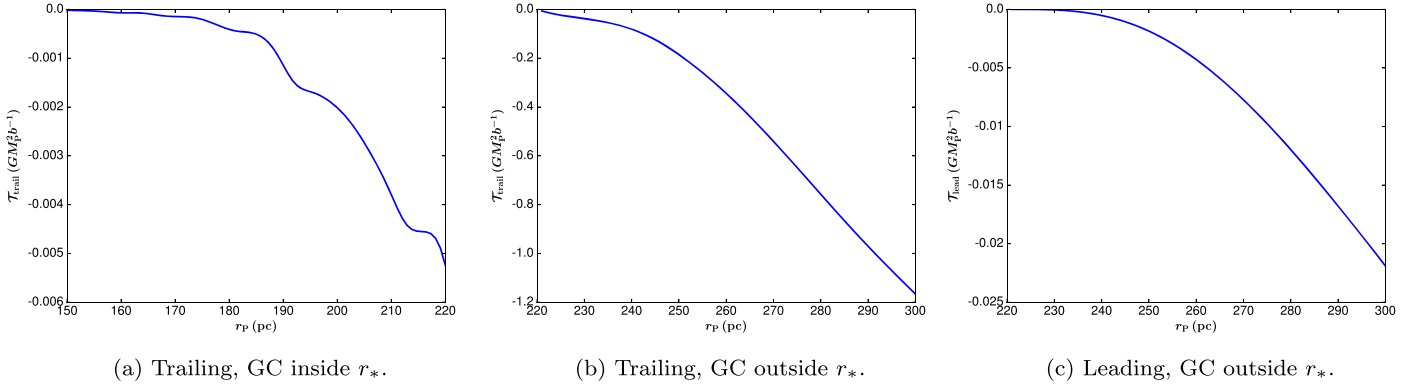
We note that X_2 is independent of (m, ℓ), whereas the ratio $X_2/X_1 = (1 + |\ell|/3m) > 1$ is independent of r_p. The resonance strength factor is

$$\mathcal{F}_{m\ell m}(r_p) = \frac{m}{3}\int_0^{X_1} dY\, A(X_r, Y)P_{m\ell m}(X_r, Y). \tag{77}$$

As $r_p \to r_*$, the upper limit of integration, $X_1 \propto |\Delta| \to 0$, and all the $\mathcal{F}_{m\ell m}$ vanish.

We calculated $\mathcal{F}_{m\ell m}(r_p)$ for all 110 resonances with $1 \leqslant m \leqslant 10$ and $-10 \leqslant \ell \leqslant 0$. Substituting these in Equation (60), we obtained the corresponding $\mathcal{T}_{m\ell m}(r_p)$. The six panels of Figure 6 track the leading resonances with $|\mathcal{T}_{m\ell m}(r_p)| > 10^{-5}$ (GM_p^2/b), for $r_* \leqslant r_p < 300$ pc. Then, $\mathcal{T}_{\mathrm{lead}}(r_p)$ was calculated by summing over $\mathcal{T}_{m\ell m}(r_p)$, as given in Equation 64(b). As in the case of the trailing torques discussed in Section 5.1.2, there is a progressive loss of resonances and torque strengths as r_p decreases. But the leading resonances are fewer in number and weaker. Here $(2, 0)$ and $(2, -2)$ are the dominant resonances throughout the range of r_p.

1. At $r_p = 300$ pc, there are 18 resonances, with $10^{-5}(GM_p^2/b) < |\mathcal{T}_{m\ell m}| \lesssim 10^{-2}(GM_p^2/b)$. The net torque due to all resonances is $\mathcal{T}_{\mathrm{lead}} \simeq -2 \times 10^{-2}(GM_p^2/b)$.

(a) Trailing, GC inside r_*.   (b) Trailing, GC outside r_*.   (c) Leading, GC outside r_*.

Figure 7. Profiles of net trailing and leading corotating torques.

2. At $r_p = 245$ pc, there are only six resonances, with $10^{-5}(GM_p^2/b) < |\mathcal{T}_{m\ell m}| \lesssim 10^{-3.2}(GM_p^2/b)$. The net torque due to all resonances is $\mathcal{T}_{\text{lead}} \simeq -10^{-3}(GM_p^2/b)$.

3. At $r_p = 229$ pc, there is just one resonance left, $(2, 0)$, with $|\mathcal{T}_{m\ell m}| > 10^{-5}(GM_p^2/b)$. The net torque due to this, together with contributions from weaker resonances, is $\mathcal{T}_{\text{lead}} \simeq -3 \times 10^{-5}(GM_p^2/b)$.

The torque profile, $\mathcal{T}_{\text{lead}}(r_p)$, is given in Figure 7(c) and discussed in Section 6.

5.2.2. GC Inside r_*

When $r_p < r_*$, we have $\Delta > 0$, and there are no solutions of Equation (74) that lie in the unit triangle. Hence, leading resonances do not exist for $r_p < r_*$, and the associated strength factors must vanish:

$$\mathcal{F}_{m\ell m}(r_p) = 0, \quad \text{when } \ell \leqslant 0 \text{ and } r_p \leqslant r_*. \qquad (78)$$

Hence, all $\mathcal{T}_{m\ell m}(r_p) = 0$, and the net leading torque $\mathcal{T}_{\text{lead}}(r_p) = 0$ when the GC is inside r_*.[8]

6. Suppressed Dynamical Friction

6.1. Torque Profiles and Suppression Factors

The trailing and leading net torque profiles, $\mathcal{T}_{\text{trail}}(r_p)$ and $\mathcal{T}_{\text{lead}}(r_p)$, were calculated for 150 pc $\leqslant r_p \leqslant$ 300 pc by summing over $\mathcal{T}_{m\ell m}$, as discussed in Section 5. These are plotted in Figure 7, whose salient features can be understood with reference to Figures 4–6. In this section, all torque values are referred to in units of $GM_p^2 b^{-1}$.

1. Reading panels (a) and (b) of Figure 7 from right to left, we see that $|\mathcal{T}_{\text{trail}}|$ decreases from about 1.17 at $r_p = 300$ pc to about 0.22 at $r_p = 252$ pc. The curve is smooth because there are several low- and high-ℓ resonances in operation throughout, counting 43 at $r_p = 300$ pc and 35 at $r_p = 252$ pc with $|\mathcal{T}_{m\ell m}| > 10^{-5}$. The strongest of these is the $(2, 2)$, but there are a handful of others of near-comparable strengths. Here $|\mathcal{T}_{\text{trail}}|$ continues to decrease with r_p, with $|\mathcal{T}_{\text{trail}}| \simeq 6 \times 10^{-2}$ at $r_p = 237$ pc. The number of significant resonances has thinned out; there are only 24 with $|\mathcal{T}_{m\ell m}| > 10^{-5}$, of

which the $(1, 3)$ is the strongest. We are on the verge of a transition, where the low-ℓ resonances are rapidly losing strength and cease to exist for $r_p \leqslant r_* \simeq 220$ pc. Here $|\mathcal{T}_{\text{trail}}|$, which now comes from only high-ℓ resonances, is small. How small this is cannot be discerned from the left end of panel (b) but is seen to be about 5×10^{-3} from the right end of panel (a). The $|\mathcal{T}_{\text{trail}}|$ declines more rapidly inside r_*. But, in contrast to the nearly featureless behavior outside r_*, $|\mathcal{T}_{\text{trail}}|$ shows steep falls interspersed with plateaus. The reason for this is the transition to a state in which the main contribution to $|\mathcal{T}_{\text{trail}}|$ comes from just one or two resonances whose dominance is transitory. The dominant resonances inside r_* are the $(1, 5)$ just inside r_*, the $(1, 7)$ at $r_p = 185$ pc, and the $(1, 9)$ at $r_p = 164$ pc. The progressive shift to higher ℓ as r_p decreases is mainly responsible for the declining torque strength, with $|\mathcal{T}_{\text{trail}}| \simeq 1.6 \times 10^{-5}$ at $r_p = 150$ pc.

2. Panel (c) of Figure 7 shows that $|\mathcal{T}_{\text{lead}}|$ decreases smoothly as r_p decreases. When compared with panel (b), we see that $|\mathcal{T}_{\text{lead}}(r_p)| \ll |\mathcal{T}_{\text{trail}}(r_p)|$, because leading resonances are weaker and fewer in number. Similar to low-ℓ trailing resonances, the leading resonances exist only when the GC is outside r_*, with $(2, 0)$ and $(2, -2)$ being the dominant ones. At $r_p = 300$ pc, there are 18 resonances with $|\mathcal{T}_{m\ell m}| > 10^{-5}$, contributing to $|\mathcal{T}_{\text{lead}}| \simeq 2 \times 10^{-2}$. At $r_p = 245$ pc, there are only six resonances with $|\mathcal{T}_{m\ell m}| > 10^{-5}$, giving $|\mathcal{T}_{\text{lead}}| \simeq 10^{-3}$. Thereafter, the torque is highly suppressed, with $|\mathcal{T}_{\text{lead}}| \simeq 3 \times 10^{-5}$ at $r_p = 229$ pc and $|\mathcal{T}_{\text{lead}}| = 0$ at $r_p = r_*$.

The torque profiles in Figure 7 should be compared with those of the Chandrasekhar torque, $\mathcal{T}_C(r_p)$, of Figure 1(a). At $r_p = 300$ pc, the four different versions of the Chandrasekhar formula give values of $\mathcal{T}_C$ ranging between -1.14 and -1.7. At $r_p = 300$ pc, the net LBK torque is $\mathcal{T} = \mathcal{T}_{\text{trail}} + \mathcal{T}_{\text{lead}} \simeq -1.17 - 0.02 = -1.19$, and hence $\mathcal{T} \approx \mathcal{T}_C$. This is reassuring and serves as a consistency check: when several resonances of comparable strengths are active, which is the case at $r_p = 300$ pc, we expect $\mathcal{T} \approx \mathcal{T}_C$, as indeed we found. In order to demonstrate how really suppressed (inside 300 pc) both $\mathcal{T}_{\text{trail}}(r_p)$ and $\mathcal{T}_{\text{lead}}(r_p)$ are vis-à-vis $\mathcal{T}_C(r_p)$, we compare them with the solid blue curve of Figure 1(a), whose torque has the least magnitude among the four curves. In this case, $|\mathcal{T}_C|$ decreases gradually from about 1.14 at $r_p = 300$ pc to 0.6 at $r_p = r_*$ and 0.29 at $r_p = 150$ pc.

---

[8] A characteristic feature revealed in Figures 4–6 is that $\mathcal{T}_{m\ell m}(r_p)$, with (m, ℓ) both even or both odd, have larger magnitudes than those corresponding to the even–odd or odd–even cases.
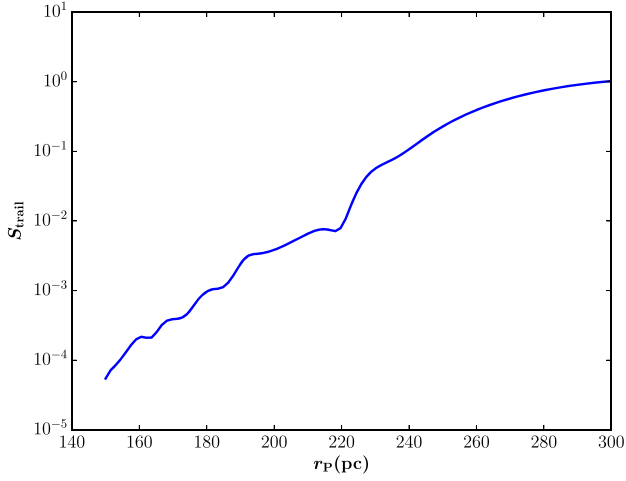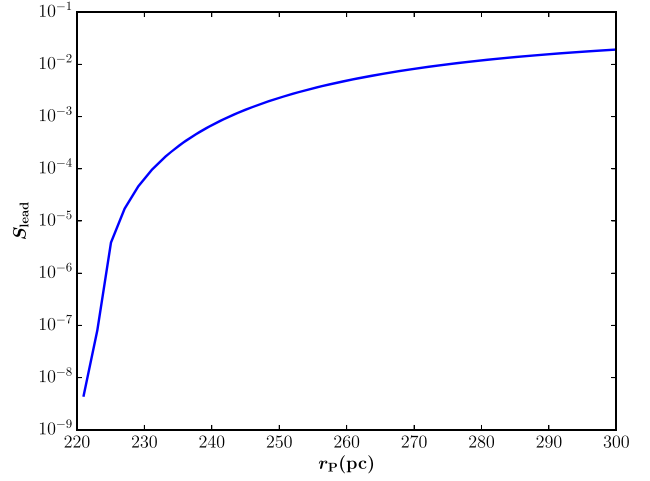
<div align="center">(a) Trailing.   (b) Leading.</div>

Figure 8. Suppression factors for trailing and leading torques.

The trailing and leading torque suppression factors,

$$S_{\text{trail}}(r_p) = \frac{\mathcal{T}_{\text{trail}}(r_p)}{\mathcal{T}_C(r_p)}, \qquad S_{\text{lead}}(r_p) = \frac{\mathcal{T}_{\text{lead}}(r_p)}{\mathcal{T}_C(r_p)}, \qquad (79)$$

are plotted in Figure 8, where it should be noted that the ordinates are displayed in a logarithmic scale. Both S_{trail} and S_{lead} decrease as r_p decreases, with $S_{\text{trail}} \gg S_{\text{lead}}$. As Figure 8(a) shows, $S_{\text{trail}} \simeq 1$ at $r_p = 300$ pc and decreases rapidly as r_p decreases. There is a steep drop as r_p approaches r_*, when the low-ℓ trailing resonances begin losing strength, that ceases to exist at $r_p = r_*$, where $S_{\text{trail}} < 10^{-2}$ is mostly due to the $(1, 3)$ and $(1, 5)$ resonances. Inside r_*, S_{trail} continues to decline rapidly, showing the steep falls and plateaus of Figure 7(a). As noted earlier, these features are due to the transitory dominance of a succession of high-ℓ resonances, the $(1, 5)$, $(1, 7)$, $(1, 9)$ etc., as r_p decreases, until $S_{\text{trail}} < 10^{-4}$ at $r_p = 150$ pc. Figure 8(b) shows S_{lead} falling steadily from 2×10^{-2} at $r_p = 300$ pc to about 6×10^{-5} at $r_p = 230$ pc, followed by a steeper decline until it vanishes at $r_p = r_*$.

6.2. Stalling of the GC's Orbit

Let us suppose that the GC was set on a circular orbit of radius $r_p = 750$ pc at some initial time. We expect that the net LBK torque, $\mathcal{T} \approx \mathcal{T}_C$ for $r_p \gtrsim 300$ pc, so $r_p(t)$ initially decays according to the Chandrasekhar formula, as discussed in Section 3.2. Figure 1(b) shows $r_p(t)$ for four different versions of $\mathcal{T}_C$. The time for r_p to decay from 750 to 300 pc varies from 5.6 to 7.3 Gyr. Thereafter, $\mathcal{T}(r_p)$ departs from $\mathcal{T}_C(r_p)$, as discussed in detail in Section 6.1. So, we must calculate further orbital decay by using the LBK torque. The equation governing $r_p(t)$ is

$$M_p \frac{d}{dt}(\Omega_p r_p^2) = \mathcal{T}(r_p) = \mathcal{T}_{\text{trail}}(r_p) + \mathcal{T}_{\text{lead}}(r_p). \qquad (80)$$

Equation (80) was integrated numerically, with the initial condition $r_p = 300$ pc at $t = 0$, using the torque profiles of Figure 7. The resulting $r_p(t) = R_{\text{LBK}}(t)$ is shown as the blue curve in Figure 9. It is evident that orbital decay is highly suppressed. We compare this with the gray curve, $r_p(t) = R_C(t)$,

for orbital decay with the most highly suppressed of the Chandrasekhar torques, used in Equation (79). For small $t < 0.5$ Gyr, the two curves overlap. This is because $\mathcal{T} \simeq \mathcal{T}_C$ near $r_p = 300$ pc. Thereafter, they depart as follows:

1. After 3 Gyr, $R_{\text{LBK}} \simeq 245$ pc, while R_C drops below r_* and reaches close to 190 pc.
2. After 6 Gyr, $R_{\text{LBK}} \simeq 235$ pc and $R_C \simeq 125$ pc. Decay slows down.
3. After 14 Gyr, R_{LBK} hovers just above r_*, while R_C has plunged to 30 pc.

The blue curve, $R_{\text{LBK}}(t)$, appears like an asymptote to $r_p = r_*$, but this is not really the case. Eventually, $r_p(t)$ will drop below r_*, because $\mathcal{T}_{\text{trail}}(r_p)$ is nonzero for $r_p < r_*$. But the timescales are much longer than is astronomically interesting.

7. Conclusions

Dynamical friction on a GC of mass $M_p = 2 \times 10^5 \, M_\odot$—set on an initially circular orbit inside an isochrone model of a dwarf galaxy—is highly suppressed when the GC's orbit enters an inner core region. For a galaxy with core radius $b = 1000$ pc and core mass $M_c = 4 \times 10^8 \, M_\odot$ (see Section 3.1.1 for choice of parameter values), this corresponds to the GC's orbital radius $r_p \leqslant 300$ pc. We found that, when $r_p = 300$ pc, the retarding LBK torque on the GC, $\mathcal{T} \approx \mathcal{T}_C$, the Chandrasekhar torque. Inside 300 pc, the LBK torque is highly suppressed because of a progressive transition to states in which there are fewer and weaker resonances in operation, so $|\mathcal{T}| \ll |\mathcal{T}_C|$. The orbital decay slows down drastically and, over astronomically interesting timescales, the GC appears to stall at a radius $r_p \gtrsim r_* \simeq 220$ pc.

In the In11 simulation, the GC's orbital decay slows down when $r_p < 300$ pc, and it appears to stall around a mean value of about 225 pc until the end of the simulation about 6 Gyr hence. In11 also studied the energy gained/lost by the stellar orbits and identified the sort of orbits that interact the strongest with the GC. Figure 10 of In11 displays some sample orbits, where it can be seen that these are nearly corotating with the GC and lagging it slightly. We found similar behavior in our calculations of torques and orbital decay in Sections 5 and 6. From Figure 9, we see that the GC's orbital decay indeed slows
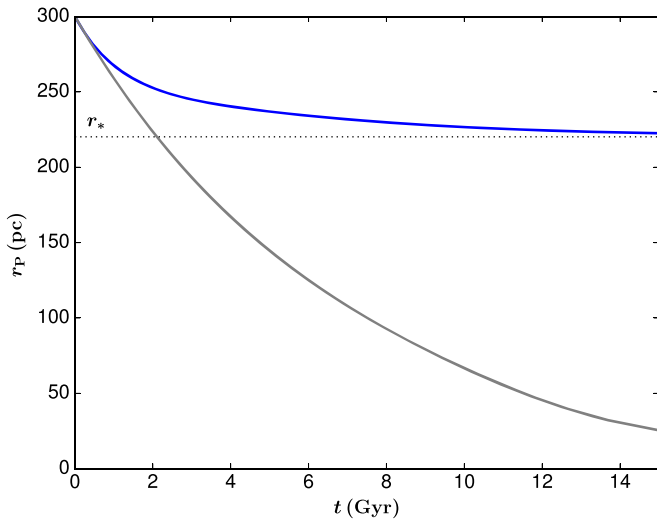
Figure 9. Orbital decay $r_p(t)$. The blue curve is for the LBK torque, and the gray curve is for the Chandrasekhar torque discussed in the text.

down inside 300 pc, with $r_p \simeq 245$ pc after 3 Gyr, and does not reach r_* even after 14 Gyr. Moreover, the strongest torques are exerted by trailing corotating resonances.

The close agreement between the stalling radius in In11 and the range 245–220 pc we obtained is somewhat fortuitous, because the isochrone and Burkert density profiles behave differently near the center. The isochrone has an analytic core density profile, $\rho_0(r) \simeq \rho_0(0)[1 - 5r^2/3b^2]$ for $r \ll b$, falling quadratically with r. The Burkert has a nonanalytic core density profile, $\rho_B(r) \simeq \rho_c [1 - r/r_c]$ for $r \ll r_c$, which falls linearly with r; the three-dimensional density gradient is singular at the origin. The corresponding mass profiles are $M_0(r) \simeq (4\pi/3)\rho_0(0)r^3$ $[1 - r^2/b^2]$ and $M_B(r) \simeq (4\pi/3)\rho_c r^3 [1 - 3r/4r_c]$. Solving Equation (55),

$$r_* \simeq \left(\frac{M_p}{M_c}\right)^{1/5} b \simeq 220 \text{ pc}, \qquad \text{isochrone,} \qquad (81a)$$

$$r_* \simeq \left(\frac{4M_p}{3M_c}\right)^{1/4} r_c \simeq 160 \text{ pc}, \qquad \text{Burkert,} \qquad (81b)$$

where M_c is the core mass of Equation (39).

The Burkert profile has a smaller r_* because its mass deficit, defined in Equation (55), increases more strongly with r. For the isochrone, the "stalling" radius $\lesssim 240$ pc is not too far away from its $r_* \simeq 220$ pc. But why does the GC in the In11 simulation appear to stall at ~ 225 pc, which is about halfway between 300 pc and the Burkert's $r_* \simeq 160$ pc? The first step toward addressing this question would be to repeat the calculations of this paper for the Burkert profile and see how resonances drop off and torques weaken as r_p drops below 300 pc. Some differences can surely be expected, because $\rho_B(r)$ is nonanalytic at the center and falls steeper than $\rho_0(r)$. But this would probably not encompass the entire story.

Figure 13 of In11 plots energy transfer—which is proportional to the angular momentum transfer—between the stars and the GC. Most of the stars absorb angular momentum from the GC, whereas a very small fraction of the stars (a few thousand out of 10 million) lose angular momentum to the GC. The former behave like the stars we studied in this paper; they absorb angular momentum from the GC and contribute to the net retarding LBK torque in proportion to the resonant torque

strengths. But the latter population—referred to as "horn particles" in In11—cannot be so described because, in the linear theory, angular momentum is always absorbed by the stars for any galaxy with DF $F(E)$ with $(dF/dE) < 0$. In Figure 13 of In11, the two populations of stars are seen to exert almost equal and opposite torques on the GC, so that the total torque is effectively zero. How do we understand this in terms of our exploration of resonances in the inner core of the isochrone?

Our calculations are a direct application of the LBK torque formula of TW84, which is derived from the linear theory of the collisionless Boltzmann equation (CBE). In order to describe the "horn particles," it is necessary to go beyond linear theory and take into account the nonlinear theory of adiabatic capture into resonance, which is discussed in TW84. Nonlinear corrections to the CBE create "islands" in the neighborhood of resonant surfaces in phase space. An isolated island consists of ("captured") orbits librating about a parent resonant orbit and bounded by separatrices on which the libration period is infinite.[9] The "horn particles" in In11 must be a population of stars captured in one or more resonant islands in phase space. Only a small fraction of the stars are "horn particles" because resonant islands occupy small phase volumes, of order the square root of the perturbation. As the GC's orbit decays, the locations of resonant surfaces in (I, L) space will drift slowly with time, as will the sizes and shapes of the resonant islands.

For well-separated resonant islands, the nonlinear perturbation to the galaxy's DF can be calculated using the theory of Sridhar & Touma (1996). Such a calculation must demonstrate that the captured stars lose angular momentum to the GC, thereby pushing it away so that it stalls somewhat farther away from r_*, nearer to 300 pc, as seen in In11. We recall from TW84 that, when many resonances of comparable strengths are active, the net effect is incoherent, so the LBK torque is reasonably approximated by the Chandrasekhar torque. In contrast, when only a few trailing corotating resonances dominate—as in the inner core region—the net effect could be cooperative, as suggested in In11. We have seen that the LBK torque itself is highly suppressed, so the oppositely directed torque due to the small number of resonantly captured stars may well suffice to cancel it. Then the galaxy and GC will no longer exert torque on each other, and we would have an approximate self-consistent solution of the CBE describing the galaxy and GC locked in a state of frictionless corotation.

Appendix
Fourier Coefficients of the Tidal Potential of the GC

The Fourier coefficients $\widetilde{\Phi}_{n\ell m}$ of the tidal potential Φ_p of the GC are given as in Equation (46),

$$\widetilde{\Phi}_{n\ell m}(I, L, L_z) = \oint \frac{dw}{2\pi} \frac{dg}{2\pi} \frac{dh}{2\pi} \Phi_p(w, g, h; I, L, L_z)$$
$$\times \exp\{-i(nw + \ell g + mh)\}, \qquad (82)$$

in terms of a three-dimensional Fourier integral over the angles (w, g, h). For corotating resonances $n = m$, so w and h occur only in the combination $w + h$. Transforming to new integration variables, (w', g, k), where $w' = w + h$ and

---

[9] Beyond the separatrices are ("free") circulating orbits that are reasonably well described by the linear CBE underlying the calculation of the LBK torque.

$k = -h$, we get

$$\widetilde{\Phi}_{m\ell m}(I, L, L_z) = \oint \frac{dw'}{2\pi} \frac{dg}{2\pi} \langle \Phi_p \rangle_k$$
$$\times \exp\{-i(mw' + \ell g)\}, \qquad (83)$$

where

$$\langle \Phi_p \rangle_k = \oint \frac{dk}{2\pi} \Phi_p \qquad (84)$$

is the k-averaged tidal potential. Below, we show that this can be evaluated analytically for core orbits. Then, $\widetilde{\Phi}_{m\ell m}$ is given as a two-dimensional Fourier transform over the w' and g of a known function. The Fourier integrals were evaluated numerically using Mathematica with a relative tolerance of 1%. Integrals of small magnitudes converge slowly when the relative error is specified, so we used absolute tolerances of 10^{-6} and 10^{-8} for $r_p > r_*$ and $r_p < r_*$, respectively.

Calculation of $\langle \Phi_p \rangle_k$. Let (x, y, z) be Cartesian coordinates in the rotating frame in which the GC is quasi-stationary. Without loss of generality, we assume that the GC lies on the x-axis. Then, the tidal potential of Equation (43) is

$$\Phi_p = -GM_p \left[\frac{1}{\sqrt{a^2 + r_p^2 + r^2 - 2r_p x}} - \frac{r_p x}{(a^2 + r_p^2)^{3/2}} \right]. \qquad (85)$$

For core orbits, Equation (49) gives

$$r^2 \simeq \frac{I}{\Omega_b}[1 - e\cos(2w)], \qquad (86a)$$

$$x \simeq \sqrt{\frac{I}{\Omega_b}} [\sqrt{1 - e}\, C_w(C_g C_h - S_g S_h C_i)$$
$$- \sqrt{1 + e}\, S_w (S_g C_h + C_g S_h C_i)], \qquad (86b)$$

where $C \equiv$ cosine and $S \equiv$ sine. Using these in Equation (85), Φ_p can be expressed in terms of action-angle variables. The next task is to express quantities in terms of (w', g, k) and average Φ_p over k. It is more convenient, and mathematically equivalent, to average over the angle $\beta = 2k + w'$, instead of over k. Rewriting

$$r^2 \simeq \frac{I}{\Omega_b}(1 - e\, C_{w'}C_\beta + e\, S_{w'}S_\beta), \qquad (87a)$$

$$x \simeq \sqrt{\frac{I}{\Omega_b}} \left[\frac{\sqrt{1-e}}{2}(C_g C_{w'} - S_g S_{w'} C_i) \right.$$
$$- \frac{\sqrt{1+e}}{2}(S_g S_{w'} - C_g C_{w'} C_i)$$
$$+ \frac{1}{2} C_g C_\beta (\sqrt{1-e} - \sqrt{1+e}\, C_i)$$
$$\left. + \frac{1}{2} S_g S_\beta(\sqrt{1-e}\, C_i - \sqrt{1+e}\,) \right], \qquad (87b)$$

we have

$$a^2 + r_p^2 + r^2 - 2r_p x \simeq A + B C_\beta + D S_\beta, \qquad (88)$$

where A, B, and D are β-independent functions, given by

$$A = a^2 + r_p^2 + \frac{I}{\Omega_b} + r_p\sqrt{\frac{I}{\Omega_b}} [\sqrt{1 + e}\, \{S_g S_{w'} - C_g C_{w'} C_i\}$$
$$- \sqrt{1 - e}\, \{C_g C_{w'} - S_g S_{w'} C_i\}], \qquad (89a)$$

$$B = -e\, C_{w'}\frac{I}{\Omega_b} - r_p\sqrt{\frac{I}{\Omega_b}}\, C_g \{\sqrt{1 - e} - \sqrt{1 + e}\, C_i\}, \qquad (89b)$$

$$D = e\, S_{w'}\frac{I}{\Omega_b} - r_p\sqrt{\frac{I}{\Omega_b}}\, S_g \{\sqrt{1 - e}\, C_i - \sqrt{1 + e}\,\}. \qquad (89c)$$

Then, the integral

$$\mathcal{I}_1 = \int_0^{2\pi} \frac{dk}{2\pi} \frac{1}{\sqrt{a^2 + r_p^2 + r^2 - 2r_p x}}$$
$$\simeq \int_0^{2\pi} \frac{d\beta}{2\pi} \frac{1}{\sqrt{A + B C_\beta + D S_\beta}}. \qquad (90)$$

Using Equation (2.580(1)) of Gradshteyn & Ryzhik (2007), we have

$$\mathcal{I}_1 \simeq \frac{2}{\pi\sqrt{A + \sqrt{B^2 + D^2}}} \mathcal{K}\left(\frac{2\sqrt{B^2 + D^2}}{A + \sqrt{B^2 + D^2}}\right), \qquad (91)$$

where

$$\mathcal{K}(s) = \int_0^{\pi/2} d\theta \frac{1}{\sqrt{1 - s\sin^2\theta}} \qquad (92)$$

is the complete elliptic integral of the first kind. We also need

$$\oint \frac{dk}{2\pi} x = \oint \frac{d\beta}{2\pi} x \simeq \frac{1}{2}\sqrt{\frac{I}{\Omega_b}} [\sqrt{1 - e}\, (C_g C_{w'} - S_g S_{w'} C_i)$$
$$- \sqrt{1 + e}\, (S_g S_{w'} - C_g C_{w'} C_i)]. \qquad (93)$$

Therefore, the k-averaged tidal potential is

$$\langle \Phi_P \rangle_k \simeq GM_p \left[-\frac{2}{\pi\sqrt{A + \sqrt{B^2 + D^2}}} \mathcal{K}\left(\frac{2\sqrt{B^2 + D^2}}{A + \sqrt{B^2 + D^2}}\right) \right.$$
$$+ \frac{r_p}{2}\sqrt{\frac{I}{\Omega_b(a^2 + r_p^2)^3}} \{\sqrt{1 - e}\, (C_g C_{w'} - S_g S_{w'} C_i)$$
$$\left. - \sqrt{1 + e}\, (S_g S_{w'} - C_g C_{w'} C_i)\} \right]. \qquad (94)$$

References

Binney, J., & Tremaine, S. 2008, Galactic Dynamics (2nd ed.; Princeton, NJ: Princeton Univ. Press)
Buonanno, R., Corsi, C. E., Castellani, M., et al. 1999, AJ, 118, 1671
Buonanno, R., Corsi, C. E., Zinn, R., et al. 1998, ApJL, 501, L33
Burkert, A. 1995, ApJL, 447, L25
Chandrasekhar, S. 1943, ApJ, 97, 255
Cole, D. R., Dehnen, W., Read, J. I., & Wilkinson, M. I. 2012, MNRAS, 426, 601

Durrell, P. R., Harris, W. E., Geisler, D., & Pudritz, R. E. 1996, AJ, 112, 972
Goerdt, T., Moore, B., Read, J. I., Stadel, J., & Zemp, M. 2006, MNRAS, 368, 1073
Gradshteyn, I. S., & Ryzhik, I. M. 2007, Table of Integrals, Series, and Products (7th ed.; Burlington, MA: Elsevier Academic Press)
Greco, C., Clementini, G., Catelan, M., et al. 2007, ApJ, 670, 332
Gualandris, A., & Merritt, D. 2008, ApJ, 678, 780
Hénon, M. 1959a, AnAp, 22, 126
Hénon, M. 1959b, AnAp, 22, 491
Hénon, M. 1960, AnAp, 23, 474
Hernandez, X., & Gilmore, G. 1998, MNRAS, 297, 517
Inoue, S. 2009, MNRAS, 397, 709
Inoue, S. 2011, MNRAS, 416, 1181
Kalnajs, A. J. 1971, ApJ, 166, 275
Kalnajs, A. J. 1972, in IAU Coll. 10, Gravitational N-Body Problem, ed. M. Lecar (Dordrecht: Reidel), 13
Lotz, J. M., Miller, B. W., & Ferguson, H. C. 2004, ApJ, 613, 262
Lynden-Bell, D., & Kalnajs, A. J. 1972, MNRAS, 157, 1
Mackey, A. D., & Gilmore, G. F. 2003, MNRAS, 340, 175
Miller, B. W., Lotz, J. M., Ferguson, H. C., Stiavelli, M., & Whitmore, B. C. 1998, ApJL, 508, L133
Murray, C. D., & Dermott, S. F. 1999, Solar System Dynamics (Cambridge: Cambridge Univ. Press)
Oh, K. S., Lin, D. N. C., & Richer, H. B. 2000, ApJ, 531, 727
Petts, J. A., Read, J. I., & Gualandris, A. 2016, MNRAS, 463, 858
Read, J. I., Goerdt, T., Moore, B., et al. 2006, MNRAS, 373, 1451
Sridhar, S., & Touma, J. 1996, MNRAS, 279, 1263
Strader, J., Brodie, J. P., Forbes, D. A., Beasley, M. A., & Huchra, J. P. 2003, AJ, 125, 1291
Strigari, L. E., Bullock, J. S., Kaplinghat, M., et al. 2008, Natur, 454, 1096
Tremaine, S., & Weinberg, M. D. 1984, MNRAS, 209, 729
Tremaine, S. D. 1976, ApJ, 203, 345
Vesperini, E. 2000, MNRAS, 318, 841
Vesperini, E. 2001, MNRAS, 322, 247
Weinberg, M. D. 1986, ApJ, 300, 93
Weinberg, M. D. 1989, MNRAS, 239, 549